UC Riverside

UC Riverside Electronic Theses and Dissertations

Title

Experimental Investigation of Acoustic Phonon Confinement Effects in Nanostructured Materials

Permalink

https://escholarship.org/uc/item/88c5800c

Author

Kargar, Fariborz

Publication Date

2016

Peer reviewed|Thesis/dissertation

eScholarship.org Powered by the California Digital Library
University of California

UNIVERSITY OF CALIFORNIA
RIVERSIDE

Experimental Investigation of Acoustic Phonon Confinement Effects in Nanostructured Materials

A Dissertation submitted in partial satisfaction
of the requirements for the degree of

Doctor of Philosophy

in

Electrical Engineering

by

Fariborz Kargar

December 2016

Dissertation Committee:
Dr. Alexander A. Balandin, Chairperson
Dr. Roger K. Lake
Dr. Alexander G. Khitun

Copyright by
Fariborz Kargar
2016

The Dissertation of Fariborz Kargar is approved:

_____

_____

_____

Committee Chairperson

University of California, Riverside

Acknowledgements

I would like to express my utmost gratitude to my PhD advisor, Dr. Alexander A. Balandin for his guidance through my research. Indeed, he was the source of inspiration who always encouraged me to carry on even at the times of disappointment. More importantly, I would like to thank him because of all the useful discussions we had during his coffee offerings, freedom in doing research and involving me in different fields of studies. It was him who granted me many opportunities to attend several conferences and meet many experts in thermal field, спасибо (thank you). I hope I had a part in breaking "another brick in the wall" of unknowns.

I also would like to thank Dr. Roger Lake and Dr. Alexander Khitun for serving as members in my dissertation committee. I was very fortunate to collaborate with them and their group members during my graduate program.

I want to express my utmost gratitude to Dr. Alexander N. Korotkov. I learned a lot from him and it was him who showed me the new exciting horizons in quantum mechanics and solid state physics. I really appreciate his after-class hours for students when he patiently explained and answered all my questions.

Many thanks to Dr. Filippo Scarponi from JRS company who corresponded my emails in detail at the times of having difficulties with Brillouin-Mandelstam light scattering instrument. It was him who changed the endless sufferings of running this instrument to "Felicita" (happiness).

I am especially thankful to my friend and "brother in arm" Bishwajit Debnath from Dr. Roger Lake's research group. Without his help, I could have not fulfilled theoretical

support to my experimental findings. May our friendship last forever, তোমাকে ধন্যবাদ (thank you).

Also, I would like to thank Dr. Denis Nika (спасибо), Dr. Monica Lacerda (obrigado) and Dr. Guanxiong Liu (谢谢) for our fruitful discussions.

Many thanks to Joona-Pekko Kakko, Dr. Antti Säynätjoki and Dr. Harri Lipsanen from Aalto University, Finland for providing us with high quality samples for my experiments.

Without the help of my colleagues at Phonon Optimized Engineered Materials (POEM) Center, I could have not completed my research. Thank you all for your help and support.

My sincerest gratitude goes to my dearest friend and my "mystic queen" Zahra Barani Beiranvand (spouse) for her support and patience during this journey. Without her love and dedication, to reach to the end of this road would be impossible. And last but not least, I would like to thank my parents (Bahman and Roghiyeh) for their "a thousand kisses deep" love and my brother (Mehrdad) for his encouragement; how I "wish you were here".

The text of this dissertation, in part or in full, is a reprint of the material as it appears in the following journals:

- Journal of Applied Physics. Reprinted with permission from Kargar, F. et al. Acoustic phonon spectrum and thermal transport in nanoporous alumina arrays. Appl. Phys. Lett. 107, 171904 (2015). Copyright 2016 AIP Publishing LLC.

- Journal of Nature Communications. Reprinted from Kargar, F. et al. Direct observation of confined acoustic phonon polarization branches in free-standing semiconductor nanowires. Nat. Commun. 7, 13400 (2016).

The co-author A. A. Balandin, listed in the above publications directed and supervised the research which forms the basis for this dissertation. This work was supported as part of the Spins and Heat in Nanoscale Electronic Systems (SHINES), an Energy Frontier Research Center funded by the U.S. Department of Energy, Office of Science, Basic Energy Sciences (BES) under Award # SC0012670. The preparation of GaAs nanowires at Aalto University was supported by Aalto University's Energy Efficiency project Moppi and by Tekes NP-NANO project.

Dedicated to

My wife

Zahra Barani Beiranvand

My parents

Bahman and Roghiyeh

And my lovely brother

Mehrdad

ABSTRACT OF THE DISSERTATION

Experimental Investigation of Acoustic Phonon Confinement Effects in Nanostructured Materials

by

Fariborz Kargar

Doctor of Philosophy, Graduate Program in Electrical Engineering
University of California, Riverside, December 2016
Dr. Alexander A. Balandin, Chairperson

This dissertation is focused on experimental investigation of confined acoustic phonons in nanostructures. Similar to electron waves, the phonon states in semiconductors can undergo changes induced by external boundaries. However, despite strong scientific and practical importance, conclusive experimental evidence of confined acoustic phonon polarization branches in individual freestanding nanostructures is lacking. In addition, the length scale at which the phonon confinement effects start to appear is a point of debate. In this dissertation, I report results of Brillouin – Mandelstam light scattering spectroscopy for two distinct material systems: nanoporous alumina films and GaAs nanowire arrays. A combined investigation of thermal conductivity and acoustic phonon spectra was conducted with nanoporous alumina membranes with the pore diameter decreasing from D=180 nm to 25 nm. The Brillouin-Mandelstam spectroscopy measurements revealed bulk-like phonon spectrum in the samples with D=180-nm pores and spectral features,

which were attributed to spatial confinement, in the samples with 25-nm and 40-nm pores. The velocity of the longitudinal acoustic phonons was reduced in the samples with smaller pores. Analysis of the experimental data and calculated phonon dispersion suggested that both phonon-boundary scattering and phonon spatial confinement affect heat conduction in membranes with the feature sizes D<40 nm. Results of the Brillouin – Mandelstam light scattering spectroscopy revealed multiple confined acoustic phonon polarization branches in GaAs nanowires with a diameter as large as 128 nm, at a length scale that exceeds the grey phonon mean-free path in this material by almost an order-of-magnitude. The dispersion modification and energy scaling with diameter in individual nanowires have been found in excellent agreement with theory. The phonon confinement effects result in a decrease in the phonon group velocity along the nanowire axis and changes in the phonon density of states. The obtained results can lead to more efficient nanoscale control of acoustic phonons, with benefits for nanoelectronic, thermoelectric and spintronic devices.

Contents

List of Figures

List of Tables

Chapter 1

Introduction and Overview

1.1 Introduction

An ability for tuning heat fluxes at nanometer scale offers tremendous benefits for heat removal from the state-of-the-art integrated circuits (ICs) and for increasing efficiency of the thermoelectric (TE) energy conversion. There is growing realization among researchers that effective control of thermal conduction in nanostructures should rely not only on the phonon – boundary scattering, but also on the spatially induced modification of the acoustic phonon spectrum[1–10]. The theory predicted that spatial confinement of the acoustic phonons – the main heat carriers in electrical insulators and semiconductors – changes the phonon scattering rates leading to the corresponding modification of the thermal conductivity[1,11,12]. Recent experiments demonstrated that the decrease of the thermal conductivity in nanowires, at least in some cases, cannot be accounted for by the phonon – boundary scattering under an assumption of the bulk acoustic phonon dispersion[3]. The conclusion in Ref. [3] was that the acoustic phonon spectrum has to be modified by the boundaries in order to lead to a strong suppression of the phonon heat conduction[3]. From the other side, there is a growing number of reports showing modification of the acoustic phonon spectrum in nanostructures measured using the Brillouin-Mandelstam light scattering spectroscopy (BMS)[13–20].

The changes in the acoustic phonon dispersion can be induced either via the stationary boundary conditions in the individual nanostructures, e.g. free-standing nanowires or suspended thin films, or via the periodic boundary conditions, e.g. superlattices. The length scale at which acoustic phonon dispersion should undergo modification and reveal itself at room temperature (RT) is a subject of debates. The traditional metric related to the phonon mean free path (MFP), Λ, determined from the expression $\Lambda = 3K/C_p\upsilon$ (here K is the phonon thermal conductivity, C_p is the specific heat and υ is the phonon group velocity) has been questioned. The reason is that Λ depends strongly on the phonon wavelength, λ, and the long-wavelength phonons can carry a much larger fraction of heat than it was previously believed[21,22]. These considerations make the study of the spatially induced modification of acoustic phonons spectrum in freestanding nanostructures important. For this reason, in the current dissertation, we will focus on direct observation of phonon confinement effects in individual nanostructures and the length scale at which they start to reveal using Brillouin-Mandelstam light scattering technique. In the next section, the outline of the dissertation is presented.

1.2 Outline of the dissertation

This dissertation is divided into the following chapters:

- Chapter 2: In this chapter, the basics of Brillouin-Mandelstam light scattering is introduced. BMS has been used extensively in this study and

this chapter will provide fundamental information about this specific technique.

- Chapter 3: This chapter presents the results of combined study of BMS on nanoporous alumina membranes and thermal conductivity measurements of samples with different pore diameters but same porosity. The goal in this chapter is to correlate the changes in the thermal conductivity of nanoporous alumina with the pore size variation to the phonon confinement effects and phonon-boundary scattering.
- Chapter 4: In this chapter, the results of BMS of free-standing GaAs nanowires are presented. This chapter conclusively demonstrates that the confinement effects appear at the length scales much larger than phonon grey (average) mean free path.
- Chapter 5: A summary of the dissertation is presented in this chapter.

References

1. Balandin, A. A. & Nika, D. L. Phononics in low-dimensional materials. *Mater. Today* **15,** 266–275 (2012).

2. Ponomareva, I., Srivastava, D. & Menon, M. Thermal conductivity in thin silicon nanowires: phonon confinement effect. *Nano Lett.* **7,** 1155–1159 (2007).

3. Wingert, M. C. *et al.* Thermal conductivity of Ge and Ge-Si core-shell nanowires in the phonon confinement regime. *Nano Lett.* **11,** 5507–5513 (2011).

4. Cuffe, J. *et al.* Phonons in Slow Motion: Dispersion Relations in Ultrathin Si Membranes. *Nano Lett.* **12,** 3569–3573 (2012).

5. Alaie, S. *et al.* Thermal transport in phononic crystals and the observation of coherent phonon scattering at room temperature. *Nat Commun* **6,** (2015).

6. Johnson, W. L. *et al.* Vibrational modes of GaN nanowires in the gigahertz range. *Nanotechnology* **23,** 495709 (2012).

7. Hu, M., Giapis, K. P., Goicochea, J. V, Zhang, X. & Poulikakos, D. Significant Reduction of Thermal Conductivity in Si/Ge Core- Shell Nanowires. *Nano Lett.* **11,** 618–623 (2010).

8. Nika, D. L. *et al.* Suppression of phonon heat conduction in cross-section-modulated nanowires. *Phys. Rev. B* **85,** 205439 (2012).

9. Li, H. *et al.* Thermal conductivity of twisted bilayer graphene. *Nanoscale* **6,** 13402–13408 (2014).

10. Fugallo, G. *et al.* Thermal conductivity of graphene and graphite: collective excitations and mean free paths. *Nano Lett.* **14,** 6109–6114 (2014).

11. Balandin, A. & Wang, K. L. Significant decrease of the lattice thermal conductivity due to phonon confinement in a free-standing semiconductor quantum well. *Phys. Rev. B* **58,** 1544 (1998).

12. Zou, J. & Balandin, A. Phonon heat conduction in a semiconductor nanowire. *J. Appl. Phys.* **89,** 2932–2938 (2001).

13. Parsons, L. C. & Andrews, G. T. Observation of hypersonic phononic crystal effects in porous silicon superlattices. *Appl. Phys. Lett.* **95,** 93–96 (2009).

14. Sato, A. *et al.* Anisotropic propagation and confinement of high frequency phonons

in nanocomposites. *J. Chem. Phys.* **130,** 111102 (2009).

15. Graczykowski, B. *et al.* Phonon dispersion in hypersonic two-dimensional phononic crystal membranes. *Phys. Rev. B* **91,** 75414 (2015).

16. Birt, D. R. *et al.* Brillouin light scattering spectra as local temperature sensors for thermal magnons and acoustic phonons. *Appl. Phys. Lett.* **102,** 82401 (2013).

17. Olsson, K. S. *et al.* Temperature dependence of Brillouin light scattering spectra of acoustic phonons in silicon. *Appl. Phys. Lett.* **106,** 51906 (2015).

18. Li, Y. *et al.* Brillouin study of acoustic phonon confinement in GeO2 nanocubes. *Appl. Phys. Lett.* **91,** 93116 (2007).

19. Parsons, L. C. & Andrews, G. T. Off-axis phonon and photon propagation in porous silicon superlattices studied by Brillouin spectroscopy and optical reflectance. *J. Appl. Phys.* **116,** 33510 (2014).

20. Sato, A. *et al.* Cavity-type hypersonic phononic crystals. *New J. Phys.* **14,** 113032 (2012).

21. Dames, C. & Chen, G. Thermal conductivity of nanostructured thermoelectric materials. *Thermoelectrics Handbook: macro to nano* (2006).

22. Yang, F. & Dames, C. Mean free path spectra as a tool to understand thermal conductivity in bulk and nanostructures. *Phys. Rev. B* **87,** 35437 (2013).

Chapter 2

Introduction to Brillouin-Mandelstam light scattering

Brillouin-Mandelstam light spectroscopy (BMS), similar to Raman light spectroscopy, is the inelastic light scattering of monochromatic laser light by phonons. While in Raman light scattering technique, it is possible to observe phonons with minimum energies of 250 GHz or higher at wave-vectors very close to Brillouin zone center, BMS can probe phonons with very low energies in the range of 2-900 GHz. Therefore, with recent technological improvements in Raman and Brillouin-Mandelstam light scattering methods, one can possibly observe phonons with few gigahertz up to several terahertz energies close to the zone center.

In this chapter, the concept of light scattering in BMS method is explained briefly. The formulas and terminology introduced in this chapter will be widely used in the succeeding chapters.

2.1 Fundamentals of Brillouin-Mandelstam light scattering spectroscopy

2.1.1 Scattering from bulk phonons

Suppose that an acoustic phonon (sound wave) with the wave-vector of **q** and frequency of ω is travelling inside the medium. Acoustic phonons propagating through a medium induce local modulations in dielectric constant ε of material from which light can be scattered[1]. Assume an incident light with the wave-length of λ_o and wave-vector $\mathbf{k_i}$

($|\mathbf{k_i}|=2\pi/\lambda_o$) enters into a material with the refractive index of n (Figure 2.1(a)). In this case, the wave-length and wave-vector of the incident light will change to λ_o/n and $\mathbf{k^*}_i$ ($|\mathbf{k^*}_i|=2\pi n/\lambda_o$), respectively. The frequency of the light will not change when entering from one medium into another. The light with the wave-vector of $\mathbf{k^*}_i$ and ω_i is scattered into the state of $\mathbf{k^*_s}$ and ω_s by the bulk (volumetric) phonons according to the following equations[1]:

$$\mathbf{k}_s^* - \mathbf{k}_i^* = \pm \mathbf{q} \tag{2.1}$$

and,

$$\omega_s - \omega_i = \pm \omega \tag{2.2}$$

(2.1) and (2.2) are the conservation of momentum and energy equations, respectively. In these equations, the "plus" and "minus" signs represents anti-stokes (absorption or annihilation) and stokes (emission) of the phonon.

Photons (incident and scattered light) have a linear dispersion and thus, the frequency of the incident and scattered light can be expressed in terms of light speed in vacuum c and the refractive index of medium n as follow:

$$\omega_s = (c/n)|\mathbf{k_s}| \tag{2.3}$$

and,

$$\omega_i = (c/n)|\mathbf{k}_i| \tag{2.4}$$

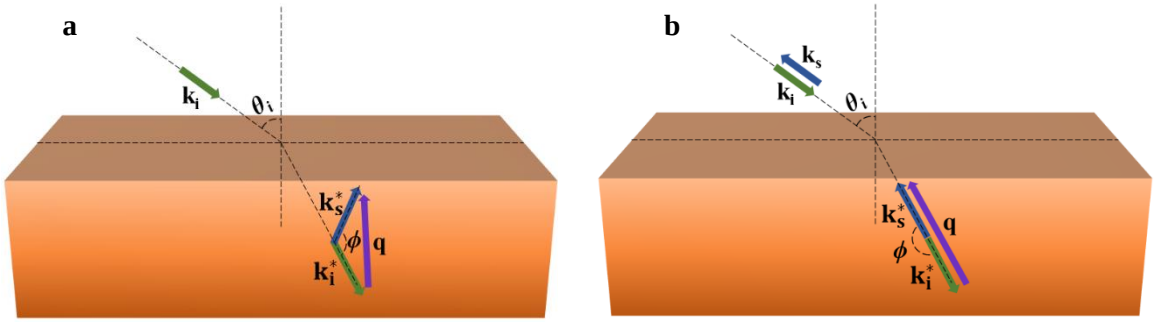

Figure 2.1. Schematic of BMS light scattering from bulk phonons. (a) General schematic of light scattering from bulk phonons. The incident and scattered light is demonstrated using arrows with green and blue colors. The purple arrow shows the acoustic phonon wave-vector. Here, ϕ is the scattering angle (angle between the incident and scattered light inside the material) which is different from the incident light angle (θ_i) (b) Schematic of the light scattering from bulk phonons in backscattering configuration. Here, the scattering angle ϕ is 180°. The backscattering configuration gives the maximum (largest) phonon wave-vector which can be probed by BMS technique from bulk phonons.

The laser light typically used in Brillouin-Mandelstam scattering has a wave-vector in the order of ~10^5 cm^{-1} which only covers a very small portion of Brillouin zone (~10^8 cm^{-1})[2]. Therefore, according to equation (2.1), the acoustic phonons with wave-vector very close to the Brillouin zone center can be probed using this technique. The acoustic phonons in the vicinity of the Brillouin zone center has a linear dispersion as follow:

$$\omega = \upsilon |\mathbf{q}| \tag{2.5}$$

in which υ is the sound velocity in the material. Thus, with respect to equations (2.3) to (2.5), equation (2.2) can be rewritten as follow:

$$\frac{|\mathbf{k_s}|-|\mathbf{k_i}|}{n|\mathbf{q}|}=\frac{|\mathbf{k}_s^*|-|\mathbf{k}_i^*|}{|\mathbf{q}|}=\frac{\upsilon}{c} \tag{2.6}$$

The order of magnitsude of υ/c is ~10^{-5} and hence, we can assume that $|\mathbf{k}_s^*|\approx|\mathbf{k}_i^*|=k$ in which $k = 2\pi n/\lambda$ and λ is the excitation laser wave-length in vacuum. Considering this and according to equation (2.1), the phonon wave-vector would be:

$$|\mathbf{q}|=(4\pi n/\lambda)\mathbf{sin}(\phi/2) \tag{2.7}$$

In this equation, ϕ is the scattering angle and has been shown in Figure 2.1 (a). In the backscattering configuration (Figure 2.1 (b)), the scattering angle ϕ is 180^o and therefore, the phonon wave-vector is:

$$|\mathbf{q}|=(4\pi n/\lambda) \tag{2.8}$$

As one can see, in backscattering geometry, phonon wave-vector is only dependent on the refractive index of scattering medium (n) and the excitation wave-length of probing laser light (λ).

2.1.2 Ripple scattering

In opaque materials and thin films, the ripples produced by the excitation laser on the surface of the sample can scatter light. High optical absorption limits the scattering

volume to the surface of the material which can affect the wave-vector conservation law. Indeed, in many cases, as materials with high absorption coefficient and thin films, ripple scattering would be the dominant scattering source. In this case, the phonon wave-vector is conserved in the direction parallel to the surface of the sample (Figure 2.2). Therefore, for the momentum conservation we can write[3]:

$$\left|\mathbf{q}_{||}\right| = \left|\mathbf{k_i}\right| \mathbf{sin}\theta_i + \left|\mathbf{k_s}\right| \mathbf{sin}\theta_s \tag{2.9}$$

in which $\mathbf{q}_{||}$ is the phonon wave vector parallel to the surface and θ_i and θ_s, are the angle of incident and scattered light with respect to the normal to the surface, respectively. In the typical backscattering geometry, $\theta_i = \theta_s = \theta$ and thus, the phonon wave vector will be:

$$\left|\mathbf{q}_{||}\right| = \left(4\pi/\lambda\right) \mathbf{sin}\theta \tag{2.10}$$

As one can see from equation (2.10), the phonon wave vector depends on laser incident angle θ and its wavelength which means that with changing the laser incident angle, one can change phonon's wave vector.

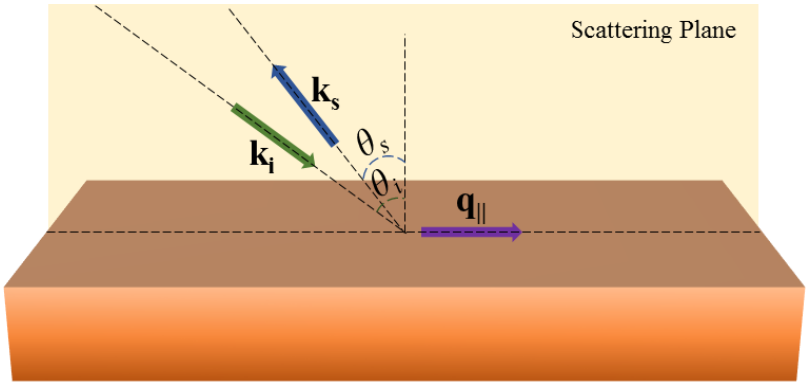

Figure 2.2. Schematic of BMS light scattering from ripple mechanism in backscattering configuration. Here, $\mathbf{k_i}$ and $\mathbf{k_s}$ are the incident and scattered light wave-vectors. The phonon wave-vector, $\mathbf{q}_{||}$, is parallel to the surface of the sample at the intersection of the "scattering plane" and sample's surface. Unlike scattering from bulk phonons, the wave-vector of the surface phonons, $\mathbf{q}_{||}$, is dependent on the incident and scattered light angles denoted by θ_i and θ_s, respectively. Usually, in the backscattering geometry, $\theta_i = \theta_s = \theta$ and therefore, $\mathbf{q}_{||}$ can be varied solely by changing the incident light angle.

2.2 Experimental Setup

Schematic of the BMS setup has been shown in Figure 2.3. In our experiments, the light source is a solid-state diode pumped laser with vertical polarization of ~100:1 and tunable power operating at λ_o =532 nm. First, the laser light passes a beam-splitter with ~95% of light transmission and ~5% of reflection. The reflected light (0.5-1 mW) is used as the reference beam which is required for stabilization and alignment of the instrument. The transmitted light passes a collimator (L1 and L2) which expands the diameter of the beam and reduces its divergence. Then, using an iris, the beam is spatially filtered. The beam is directed by mirror M1 to the Glan-polarizer. The beam leaving the Glan-polarizer is highly polarized (100000:1). Then, a half-wave plate is used in order to change the polarization of the beam. With half-wave plate, one can change the polarization of the

incident light on the sample to p-polarized (electric field polarized parallel to the plane of incidence) or s-polarized (electric field polarized perpendicular to the plane of incidence) light. Then, the light hits a partially coated mirror M2 (a very small prism can be used instead) and focused on the sample through a lens (L3) with diameter of 25.4 mm and focal distance of 35.0 mm (NA=1.4). The scattered light was collected with the same focusing lens and focused on the input-pinhole of the instrument using another lens (L4). The periscope (M3 and M4) is required for directing the focused scattered light perpendicular to the input pinhole. After that, the light enters the high-resolution six-pass tandem Fabry-Perot interferometer (JRS Instruments). A specially designed stage is able to rotate the sample up to 80^{o} relative to the direction of the incident laser light with an accuracy of 0.02^{o}. With changing the incident angle, one can choose the probing wave-vector of phonons if the scattering is dominated by ripple mechanism.

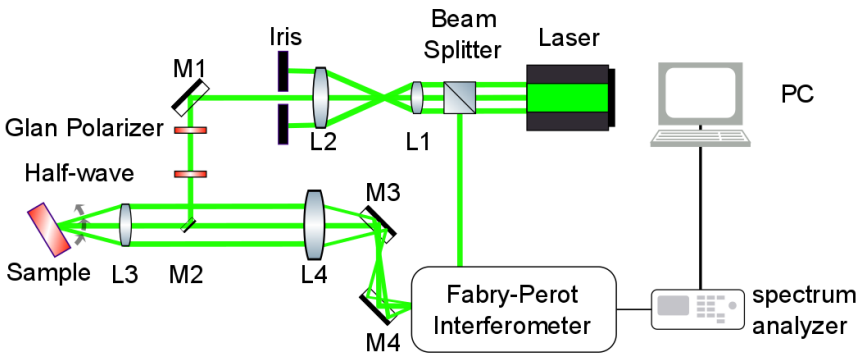

Figure 2.3. Schematic of BMS experimental setup. “M” and “L” indicate mirrors and lenses, respectively.

References

1. Sandercock, J. R. Trends in brillouin scattering: Studies of opaque materials, supported films, and central modes. *Light Scatt. Solids III* **51,** 173–206 (1982).

2. Mutti, P. *et al.* in *Advances in Acoustic Microscopy* (ed. Briggs, A.) **1,** 249–300 (Springer US, 1995).

3. Sanderocock, J. R. Light scattering from surface acoustic phonons in metals and semiconductors. *Solid State Commun.* **26,** 547–551 (1978).

Chapter 3

Brillouin-Mandelstam light scattering from nanoporous alumina

3.1 Introduction

As the first step in studying phonon confinement effects in free-standing nanostructures, we report results of a combined investigation of thermal conductivity and acoustic phonon spectra in nanoporous alumina membranes with the pore diameter decreasing from D=180 nm to 25 nm. The samples with the hexagonally arranged pores were selected to have the same porosity $\phi \approx 13\%$. The Brillouin-Mandelstam spectroscopy measurements revealed bulk-like phonon spectrum in the samples with D=180 nm pores and spectral features, which were attributed to spatial confinement, in the samples with 25-nm and 40-nm pores. We will see in this chapter that the velocity of the longitudinal acoustic phonons was reduced in the samples with smaller pores. Analysis of the experimental data and calculated phonon dispersion suggests that both phonon-boundary scattering and phonon spatial confinement affect heat conduction in membranes with the feature sizes D<40 nm.

3.2 Sample Characterization

Nanoporous alumina films studied here were membranes with the hexagonally arranged pores with the average diameter D=180 nm, 40 nm and 25 nm. The corresponding

inter-pore distances were H= 480 nm, 105 nm and 65 nm. The samples produced via the standard electrochemical technique[1] (referred below as A, B, and C) were carefully selected to have the same porosity $\phi = \pi D^2/(2\sqrt{3}H^2)$. For this set specifically, the porosity value was $\phi \approx 13\%$. The constant porosity was important because in the effective medium approximation (EMA), composite samples of the same porosity should have the same thermal conductivity[2–4]. The thickness of alumina films was in the range of 100 μm. Figure 3.1 shows the scanning electron microscopy (SEM) image of representative samples. One can see a nearly perfect periodic arrangement of the pores.

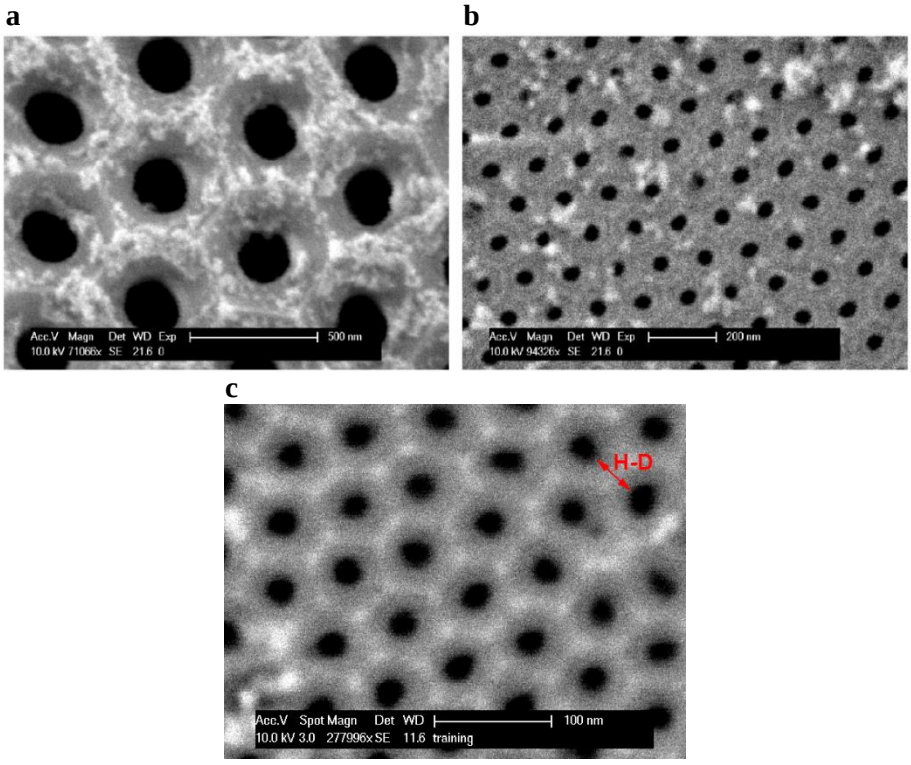

Figure 3.1. Scanning electron microscopy (SEM) image of the examined porous alumina samples with notations. (a) D = 180 nm and H = 480 nm (b) D = 40 nm and H = 105 nm (c) D = 25 nm and H = 65 nm. Figure 3.1 (c) is reprinted from Kargar, F. *et al.* Acoustic phonon spectrum and thermal transport in nanoporous alumina arrays. *Appl. Phys. Lett.* **107,** 171904 (2015), with the permission of AIP Publishing.

3.3 Thermal conductivity measurements

The measurements of the cross-plane (perpendicular to the film surface) and in-plane (along the film surface) thermal diffusivity, α, were carried out using the transient "laser flash" method (Netzsch LFA). In this technique, the bottom of the sample was illuminated by a flash of a xenon lamp. The temperature of the opposite surface of the sample was monitored with a cryogenically cooled detector. The temperature rise as a function of time was used to extract α. The in-plane measurements required a special sample holder described by us elsewhere[5]. The cross-plane thermal conductivity, K_C, and in-plane thermal conductivity, K_I, were determined from the equation $K_{C,I}=\rho\alpha_{C,I}C_p$, where ρ is the mass density and C_p is the specific heat[6]. The results for K_C are shown in Figure 3.2(a). No clear trend with temperature was observed for K_I. The measured RT values of K_I and K_C are summarized in **Table 3.1**.

Table 3.1. Experimental thermal conductivity of nanoporous alumina samples at room temperature

Sample	A: D=180 nm	B: D=40 nm	C: D=25 nm
In-Plane K (W/mK)	2.5±0.13	3.3±0.17	2.6±0.13
Cross-Plane K (W/mK)	1.1±0.05	1.0±0.05	0.9±0.05

The first interesting observation from the experimental data is that the K_C and K_I for D=25-nm and D=180-nm samples are different despite the same porosity $\phi\approx$13%. The second is that both K_C and K_I are much lower than predictions of any of the EMA models. The measured data are consistent with prior study of porous alumina that also reported K in the 0.53 W/mK - 1.62 W/mK range[7]. Our calculation of K of porous alumina using

different EMA models gave values between 12 W/mK and 30 W/mK [2–4] for the reported *K* of bulk alumina without pores, which varies from 15 to 34 $Wm^{-1}K^{-1}$ [8]. Given the small Grashof number for alumina and the considered temperature range, the convection and radiation contributions to the heat transport can be neglected[8]. The more than an order-of-magnitude deviation of the experimental *K* from EMA predictions suggests significant phonon – boundary scattering or phonon spectrum modification.

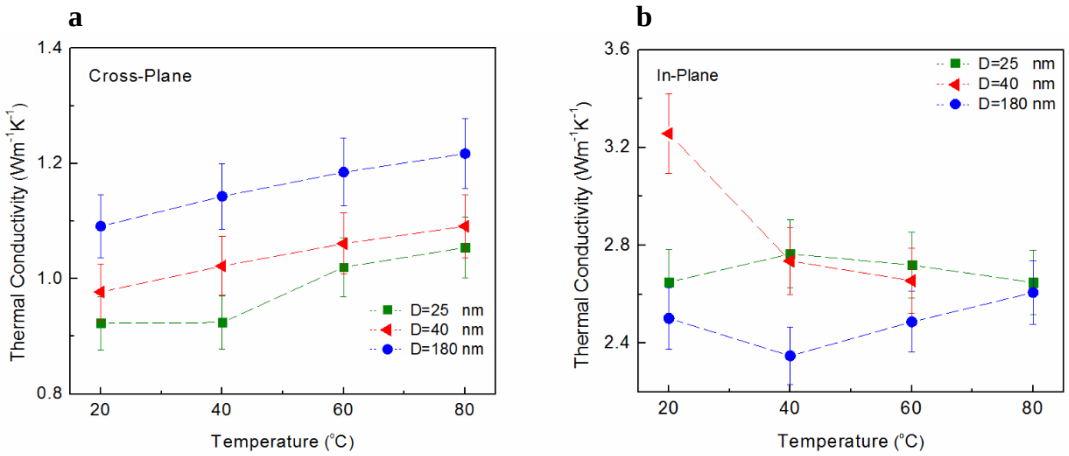

Figure 3.2. Cross-plane and in-plane thermal conductivity results of nanoporous alumina membranes with different pore diameter and inter-pore distance. (a) Cross-plane and (b) in-plane thermal conductivity of porous alumina membranes with the pore diameter D = 25 nm, D = 40 nm, D = 180 nm and corresponding inter-pore distances H = 65 nm, H = 105 and H = 480 nm. Despite large difference in feature sizes, all samples had the same porosity ϕ=13%. While cross-plane thermal conductivity decreases with decreasing the pore-size, there is no clear trend for in-plane thermal conductivity. Figure 3.2 (a) is reprinted from Kargar, F. *et al.* Acoustic phonon spectrum and thermal transport in nanoporous alumina arrays. *Appl. Phys. Lett.* **107,** 171904 (2015), with the permission of AIP Publishing.

3.4 Brillouin-Mandelstam light scattering measurements

In order to understand whether phonon spectrum modifications can possibly affect the heat conduction in these nanoporous samples, we carried out the Brillouin-Mandelstam

light scattering spectroscopy (BMS). The experimental setup was based on the six-pass tandem Fabry-Perot interferometer[13–15]. All experiments were carried out using the *p*-unpolarized backscattering mode (Figure 2.1 (b)) (the incident light is p-polarized, but the polarization of the scattered light has not been analyzed) and different laser incident angles, θ_i, ranging from 0 to 60°. The spectra were excited with the solid-state diode-pumped laser operating at λ_o=532 nm. The laser light was focused onto a sample by a lens with the numerical aperture of 1.4. The power on the sample was about 100 mW. The scattered light was collected with the same lens and directed to the Fabry-Perot interferometer.

Figure 3.3 shows BMS spectra for the nanoporous samples A, B, and C. Owing to the semi-transparent nature of our samples one can expect to observe light scattering from the bulk (i.e. volume) of the material via the elasto-optic scattering mechanism and from the surface of the film via the "ripple" scattering mechanism[15,16]. The interpretation of BMS peaks originating from the elasto-optic scattering requires an accurate knowledge of the refractive index, *n*, of the material. The refractive index was measured by the "prism-coupling" method (Metricon 2010/M)[17]. The experimental values were n=1.58 for the cross-plane direction (parallel to the pores) and n=1.55 for in-plane direction (perpendicular to the pores) at λ=532 nm. The Maxwell-Garnett approximation gave a rather close result $n = \left((1-\phi)n_m^2 + \phi n_o^2\right)^{1/2} \approx 1.54$ where n_m is the refractive index of bulk alumina without pores and n_o is the refractive index of air. For the elasto-optic scattering the interacting phonon wave vector, q, is given as $q = 4\pi n/\lambda$, which translates to q=0.0373 nm^{-1} in our case.

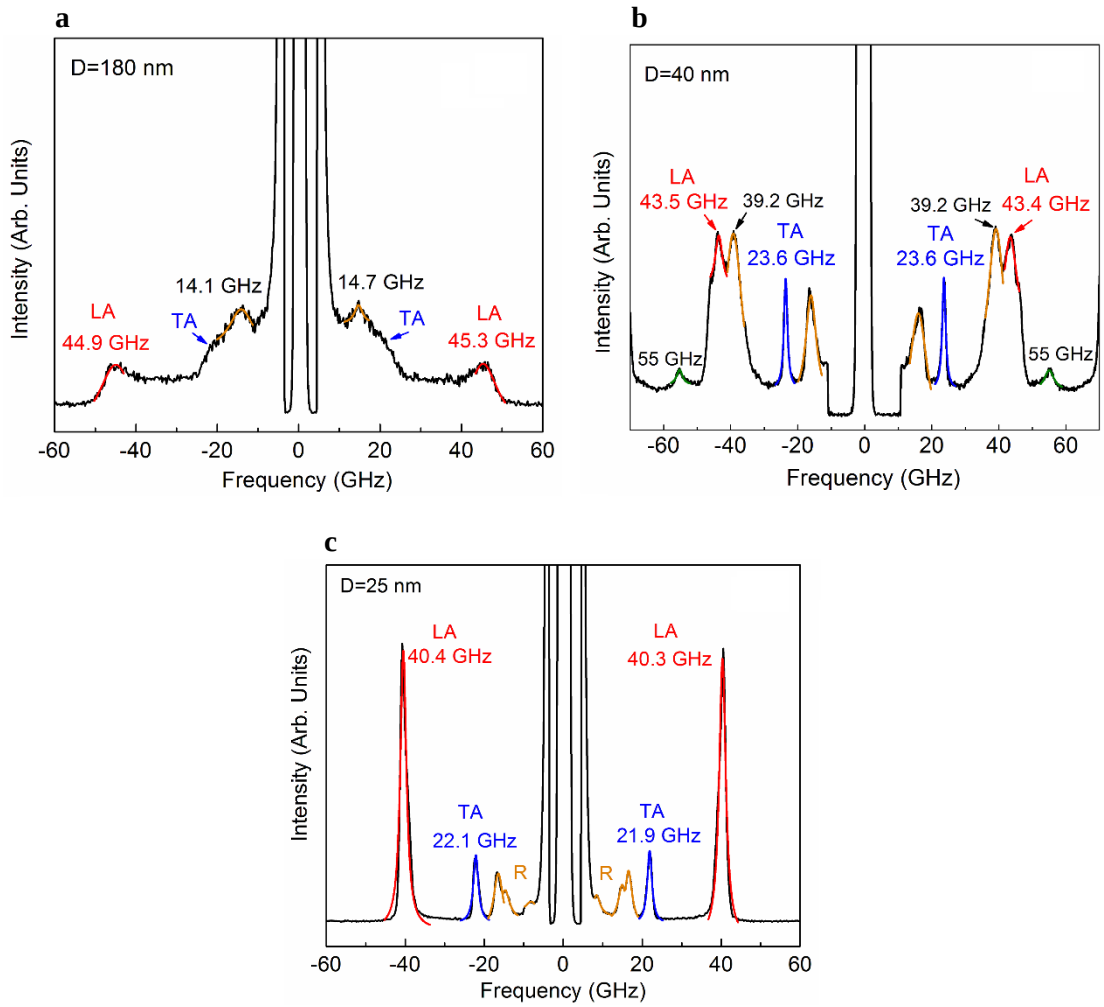

Figure 3.3. Brillouin-Mandelstam scattering spectra of nanoporous alumina samples with different pore diameter and inter-pore distances. (a) D=180 nm, (b) D=40 nm and (c) D=25 nm. The results are shown for the incident angle θ_i=40°. Note a shift in the LA and TA phonon peaks with decreasing D and H. Multiple peaks in D=25 nm sample were attributed to the "ripple" scattering peaks indicated with orange color. Reprinted from Kargar, F. *et al.* Acoustic phonon spectrum and thermal transport in nanoporous alumina arrays. *Appl. Phys. Lett.* **107,** 171904 (2015), with the permission of AIP Publishing.

3.5 Discussion

While the concept of phonons cannot be fully extended to amorphous materials, one can still talk about elastic waves and scattering of acoustic phonons in such materials[9,10]. The trend of increasing K_C with D can be rationalized by estimating the phonon – boundary scattering rate $1/\tau_B$. The heat propagates along the pores via the barrier-neck regions with the characteristic lateral dimension of H-D (see Figure 3.1 (c)). Due to periodicity of the structure all barrier-neck regions have the same dimensions. The strength of the acoustic phonon scattering can be roughly estimated from the expression[11] $1/\tau_B = \varsigma(\upsilon/(H-D))[(1-p)/(1+p)]$, where ζ is the geometrical factor related to the cross-section shape and p is the specularity parameter determined by the surface roughness. For samples with similar roughness, the ratio of the phonon – boundary scattering rate in the A and C samples, will be $\gamma = (1/\tau_B)_A/(1/\tau_B)_C \approx (\upsilon_A/\upsilon_C)((H_C-D_C)/(H_A-D_A))$. Disregarding the difference in the phonon velocity we obtain $\gamma \approx 0.13$. Optical microscopy and SEM inspection indicated that the D=180-nm sample had higher roughness. Assuming conservatively, $p \approx 0$ (diffuse scattering) for A and $p \approx 0.5$, for C, we obtain $\gamma \approx 0.39$. The latter means that the phonon – boundary scattering rate in the sample with larger pores is still smaller despite rougher surface, which translates to higher K_C. This conclusion is in line with the study of the thermal conductivity reduction in silicon membranes with hexagonally patterned nearly periodic holes with feature sizes ~ 55 nm[12].

Regarding the BMS results, one can see from Figure 3.3 (a-c) that the acoustic phonon spectrum of 180-nm sample is bulk-like. The peak at ~45 GHz was identified as the longitudinal acoustic (LA) phonon. The measured peak energy corresponds to the

phonon velocity $\upsilon_L = \omega / q = 2\pi f / q \approx 7580$ m/s (here f is the frequency of the phonon). Near the Brillouin zone (BZ) center the phonon group velocity, which defines thermal transport, coincides with the phase velocity, and it is referred to as phonon velocity in the rest of discussion. The broad shoulder at $f \approx 21$-25 GHz was attributed to the transvers acoustic (TA) phonon. The exact velocity could not have been extracted owing to its large width. BMS spectra for samples with 40-nm and 25-nm pores reveal interesting differences as compared to that of 180-nm sample. The LA phonon peak energy decreases from ~45.0 GHz in 180-nm sample to ~43.4 GHz in the 40-nm sample and ~40.4 GHz in the 25-nm sample. The velocity was extracted for the same incident light angle of $\theta_i = 40^o$ in order to avoid possible effects of the refractive index anisotropy. The LA phonon velocity in the 25-nm sample is $\upsilon_L \approx 6805$ m/s, which corresponds to ~10% reduction. The peaks in 40-nm and 25-nm samples become narrower. However, the peak width cannot be directly related to the phonon life-time in such experiments. The TA peaks in the 40-nm and 25-nm samples become pronounced and show similar reduction in the phonon velocity with decreasing structure feature size from $\upsilon_T \approx 3975$ m/s to $\upsilon_T \approx 3689$ m/s.

The observed additional peaks at the frequencies below that of TA phonon were attributed to the surface phonons interacting via the "ripple" scattering mechanism[15,16]. In the case of semi-opaque film, the light scattering occurs at or near the surface. In this case, the phonon wave vector selection rules are reduced to the component $q_{||}$ parallel to the surface. This component does not depend on n and it is given as $q_{||} = (4\pi/\lambda)\sin\theta_i$, where θ_i is the incident light angle with respect to the normal to the surface. We established that the surface phonons become visible for $\theta_i > 20^o$. The position of these peaks changes with the

incident light angle[15,16]. The position of the "volume" LA peak also can change. But the latter is explained not by the dependence of $q_{||}$ on θ_i, but rather by n anisotropy. For this reason, comparison of υ_L at the same θ_i is essential. The effect of the surface phonons on heat conduction (particularly in-plane) requires further studies.

The elasticity theory relates the phonon velocity to material parameters as $\upsilon_L = (E_L / \rho)^{1/2}$ where E_L is the longitudinal Young's modulus and ρ is the mass density. Since all considered samples had the same porosity $\phi \approx 13\%$ one would expect from EMA that υ_L should be the same. However, we observed a trend for decreasing velocity with the decreasing characteristic dimensions of the samples. This suggests that certain modification of the acoustic vibrational spectrum takes place. The elastic continuum theory predicts that the acoustic phonon confinement effects in nanostructures reveal themselves via decreased velocity of the true acoustic modes (defined as those that have $\omega(q=0)=0$) and appearance of the confined quasi-optical subbands ($\omega(q=0)\neq 0$) emanating from the same acoustic polarization branches[18–21]. The calculated dispersion for our structure in cross-plane direction is shown in Figure 3.4. The material parameters, extracted from the experimental data for bulk sample (180 nm pores), υ_L = 7580 m/s, υ_T = 3424.9 m/s and ρ = 2717.4 kg/m^3 were used in the modeling. One can see from Figure 3.4 (a) that for a given experimental q, the LA peak can consist of a mixture of phonons from several branches. However, the trend of decreasing υ_L and υ_T with reduced feature size is consistent with the experiment (see Figure 3.4 (b)).

Our BMS and computational data indicate that for a given material system, the modification of acoustic vibrational spectra became pronounced for the structures with the characteristic dimensions D=25 nm (H-D=40 nm). These dimensions are larger than averaged phonon MFP obtained from the K value. The latter supports recent theoretical considerations of stronger contributions of the long-wavelength phonons with large MFP to heat conduction in solids[22,23]. Noting that in the perturbation theory phonon scattering rate on defects is given as[24] $1/\tau_D \propto \omega^4/\upsilon^3$ one can conclude that the change in the phonon velocity can noticeably affect K.

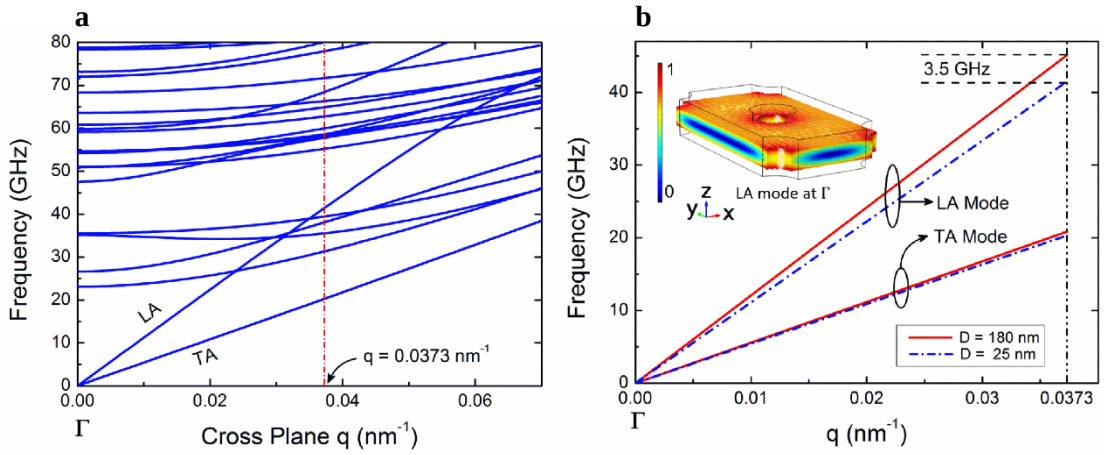

Figure 3.4. Phonon dispersion for nanoporous alumina in cross-plane direction. (a) Calculated phonon dispersion of the samples with D=25 nm and H=65 nm in cross-plane direction. (b) Dispersion of the "true acoustic" branches shown for the samples with D=180 nm ("bulk") and D=25 nm pores. Note the reduced LA and TA phonon velocity are in agreement with the experimental data. The experimentally observed LA peak frequency can also be affected by the mixing shown in (a). The inset in (b) shows displacement distribution for LA mode. Reprinted from Kargar, F. *et al.* Acoustic phonon spectrum and thermal transport in nanoporous alumina arrays. *Appl. Phys. Lett.* **107,** 171904 (2015), with the permission of AIP Publishing.

3.6 Summary

In summary, we conducted the combined study of thermal conductivity and acoustic phonon spectrum in nanoporous alumina membranes. The analysis of the obtained thermal and phonon spectrum data suggests that both phonon-boundary scattering and phonon confinement affect the heat conduction in the considered alumina nanostructures with the feature sizes D<40 nm.

References

1. Li, F., Zhang, L. & Metzger, R. M. On the growth of highly ordered pores in anodized aluminum oxide. *Chem. Mater.* **10,** 2470–2480 (1998).

2. Wang, M. & Pan, N. Predictions of effective physical properties of complex multiphase materials. *Materials Science and Engineering R: Reports* **63,** 1–30 (2008).

3. Pabst, W., Gregorová, E. & Tichá, G. Effective properties of suspensions, composites and porous materials. *J. Eur. Ceram. Soc.* **27,** 479–482 (2007).

4. Pabst, W. Simple second-order expression: For the porosity dependence of thermal conductivity. *J. Mater. Sci.* **40,** 2667–2669 (2005).

5. Goli, P. *et al.* Thermal Properties of Graphene - Copper - Graphene Heterogeneous Films. *Nano Lett.* (2014). doi:10.1021/nl404719n

6. Gregorová, E., Pabst, W., Sofer, Z., Jankovský, O. & Matějíček, J. Porous alumina and zirconia ceramics with tailored thermal conductivity. *J. Phys. Conf. Ser.* **395,** 12022 (2012).

7. Lee, J., Kim, Y., Jung, U. & Chung, W. Thermal conductivity of anodized aluminum oxide layer: The effect of electrolyte and temperature. *Mater. Chem. Phys.* **141,** 680–685 (2013).

8. Živcová, Z. *et al.* Thermal conductivity of porous alumina ceramics prepared using starch as a pore-forming agent. *J. Eur. Ceram. Soc.* **29,** 347–353 (2009).

9. Shuker, R. & Gammon, R. W. Raman-scattering selection-rule breaking and the density of states in amorphous materials. *Phys. Rev. Lett.* **25,** 222 (1970).

10. Laughlin, R. B. & Joannopoulos, J. D. Phonons in amorphous silica. *Phys. Rev. B* **16,** 2942 (1977).

11. Ziman, J. M. *Electrons and phonons: the theory of transport phenomena in solids*. (Oxford University Press, 1960).

12. Tang, J. *et al.* Holey silicon as an efficient thermoelectric material. *Nano Lett.* **10,** 4279–4283 (2010).

13. Sanderocock, J. R. Light scattering from surface acoustic phonons in metals and semiconductors. *Solid State Commun.* **26,** 547–551 (1978).

14. Sandercock, J. R. Trends in brillouin scattering: Studies of opaque materials, supported films, and central modes. *Light Scatt. Solids III* **51,** 173–206 (1982).

15. Mutti, P. *et al.* in *Advances in Acoustic Microscopy* (ed. Briggs, A.) **1,** 249–300 (Springer US, 1995).

16. Beghi, M., Every, A. & Zinin, P. in *Ultrasonic Nondestructive Evaluation* (CRC Press, 2003). doi:doi:10.1201/9780203501962.ch10

17. Onodera, H., Awai, I. & Ikenoue, J. Refractive-index measurement of bulk materials: prism coupling method. *Appl. Opt.* **22,** 1194–1197 (1983).

18. Balandin, A. & Wang, K. L. Significant decrease of the lattice thermal conductivity due to phonon confinement in a free-standing semiconductor quantum well. *Phys. Rev. B* **58,** 1544 (1998).

19. Zou, J. & Balandin, A. Phonon heat conduction in a semiconductor nanowire. *J. Appl. Phys.* **89,** 2932–2938 (2001).

20. Pokatilov, E. P., Nika, D. L. & Balandin, A. A. Acoustic-phonon propagation in rectangular semiconductor nanowires with elastically dissimilar barriers. *Phys. Rev. B* **72,** 113311 (2005).

21. Pokatilov, E. P., Nika, D. L. & Balandin, A. A. Acoustic phonon engineering in coated cylindrical nanowires. *Superlattices Microstruct.* **38,** 168–183 (2005).

22. Dames, C. & Chen, G. Thermal conductivity of nanostructured thermoelectric materials. *Thermoelectrics Handbook: macro to nano* (2006).

23. Yang, F. & Dames, C. Mean free path spectra as a tool to understand thermal conductivity in bulk and nanostructures. *Phys. Rev. B* **87,** 35437 (2013).

24. Klemens, P. G., Seitz, F. & Turnbull, D. *Solid state physics, Vol. F. Seitz and D. Turnbull (New York: Academic)* (1958).

Chapter 4

Brillouin-Mandelstam light scattering from GaAs nanowires

4.1 Introduction

The phonon states in crystal lattices can undergo changes induced by external boundaries[1,2]. Modification of the acoustic phonon spectrum in structures with periodically modulated elastic constant or mass density – referred to as phononic crystals – has been proven experimentally and utilized in practical applications[3–8]. A possibility of modifying the acoustic phonon spectrum in individual nanostructures via spatial confinement would bring tremendous benefits for controlling phonon-electron interaction and thermal conduction at the nanoscale[9–11]. Engineering electron waves and energy dispersions with external boundaries in semiconductor heterostructures and quantum well superlattices became the foundation of modern electronics and optoelectronics[11]. Recent technological developments suggest that tuning the phonon energy dispersion may become as important for the next generation of nanoelectronic circuits as engineering of the electron dispersion. Acoustic phonons carry heat in semiconductors. Improving phonon transport in nanometer scale devices is crucial for their reliability. Phonons set performance limits for alternative technologies under development, from superconducting electronics to spintronics and quantum computing[12,13].

It has long been suggested theoretically that sound waves in layered media[14], or acoustic phonons in nanostructures, can undergo modification due to externally imposed

periodic or stationary boundary conditions[15–17]. Modulation of the elastic constants, C_{ij}, or mass density, ρ, in such structures can lead to changes in the acoustic phonon dispersion, $\omega(q)$, which include reduction in the phonon group velocity, $v_G = \partial\omega(q)/\partial q$ or emergence of the phonon energy band gaps (here ω and q are the phonon energy and wave vector, respectively)[5,8,10,15–19]. There are many experimental reports of the phonon wave effects in periodic structures, including the early Raman spectroscopy studies in semiconductor superlattices[20]. The possibility of controlling the acoustic phonon spectrum in periodic structures has led to an explosive growth in the field of phononic crystals[4–8]. Despite the strong motivations, and a large body of theoretical studies[10,11], experimental investigation of the acoustic phonon confinement effects in individual nanostructures – as opposed to periodic composites – is lagging behind.

Establishing the existence of confined phonon subbands in free-standing nanostructures, and determining the length scale, D, at which they reveal themselves are important tasks. Controlling the phonon spectrum via spatial confinement would allow for fine-tuning of the phonon interactions with electrons, spins and other phonons, particularly at low temperature. A commonly used assumption in the thermal community[21,22] is that the phonon spectrum modifications only appear when the structure size is on the order of the dominant thermal phonon wave length $\lambda_T \approx (v_s h)/(k_B T)$, which is about 1.5 nm for many solids at room temperature (RT) (here k_B is the Boltzmann constant, T is the absolute temperature, h is the Planck constant, and v_s is the sound velocity). This criterion is based on the notion that the phonon wave functions do not preserve coherence over larger distances owing to natural surface roughness in real nanostructures, defects and lattice

anharmonicity. As a result, the phonon wave interference required for modification of the phonon dispersion does not take place even if solution of the elasticity equation predicts the appearance of confined phonon subbands. Another point of view[2,10,15,18] considers that phonon spatial confinement effects start to take place when D is on the order of the average phonon mean free path (MFP), defined in kinetic theory as the grey MFP: $\Lambda_G = 3K/(C_V \upsilon_s)$, which is about 20 nm for bulk GaAs at RT (here, K and C_V are the thermal conductivity and specific heat capacity, respectively). This is considered of importance because energy differences between the phonon subbands in the middle of the Brillouin zone (BZ) can result in changes in the electron – phonon scattering, and, correspondingly, electron relaxation rates, particularly at low temperature[2,12,23]. In the thermal context, the spatial confinement and modification of the phonon density of states (DOS) can affect the thermal conductivity. Recent studies established that the phonon MFP can be substantially larger than Λ_G [24–26]. It was found, that 40% of thermal conductivity of crystalline Si near RT come from the phonons with MFP above 1 μm[26]. The phonons with the longest MFP may have the lowest frequency, ω. The phonon life-time scales as $\tau \propto \omega^{-s}$, where $s \geq 1$ depends on the phonon scattering mechanism and dimensionality of the system. As a result, phonon MFP $\Lambda = \upsilon_G \tau$ will be growing with decreasing ω. The discovery of the large contribution of the long-MFP phonons to thermal conductivity makes the task of determining the length scale of the onset of confinement effects even more important.

Semiconductor NWs with smooth boundaries are the most suitable candidates for investigation of spatial confinement of acoustic phonons in the free-standing (or free-surface) nanostructures. For NWs, the characteristic length scale D is the diameter.

However, random distribution of diameters in typical NW arrays, small distances between NWs, and difficulty of direct detection of acoustic phonons so far precluded confirming the theoretically predicted confined phonon branches in NWs[27,28]. A few published reports for NWs only infer possible confinement effects indirectly by measuring thermal conductivity and comparing the result with calculations, which use both bulk and confined phonon dispersion[29,30]. This approach is ambiguous owing to the difficulty of separating the phonon confinement effects from the phonon – boundary scattering. A Brillouin spectroscopy study of GaN nanowires made an important step forward in investigating confined phonons[31]. However, a large distribution in NW diameters, and discrepancy between the experimental and calculated dispersion left the question open. A Raman spectroscopy study of the etched Si membranes gave the energies of the slab phonon modes in the BZ center[32]. Another notable investigation of the etched suspended Si membranes confirmed the changes in the fundamental phonon modes but have not shown clear confined phonon subbands, possibly owing to surface roughness inherent for the etched films or strain in the suspended structures[33].

Here, we report measurements of the acoustic phonon spectrum of NWs in a unique set of NW arrays with different diameter and large inter-nanowire distance, which allowed us to conclusively prove the existence of the confined phonon polarization branches in individual nanostructures. We have also discovered that the phonon confinement effects become pronounced at a substantially larger length scale than previously believed. Our analysis is focused on confined phonons in the 4 GHz – 40 GHz range. However, higher frequency confined phonons have also been observed. By varying the distance between the

NWs we proved that the observed spectral feature are signatures of individual NWs. The measured phonon dispersion in NWs is in excellent agreement with theory. The obtained results can lead to more efficient nanoscale control of acoustic phonons, with benefits for various practical applications.

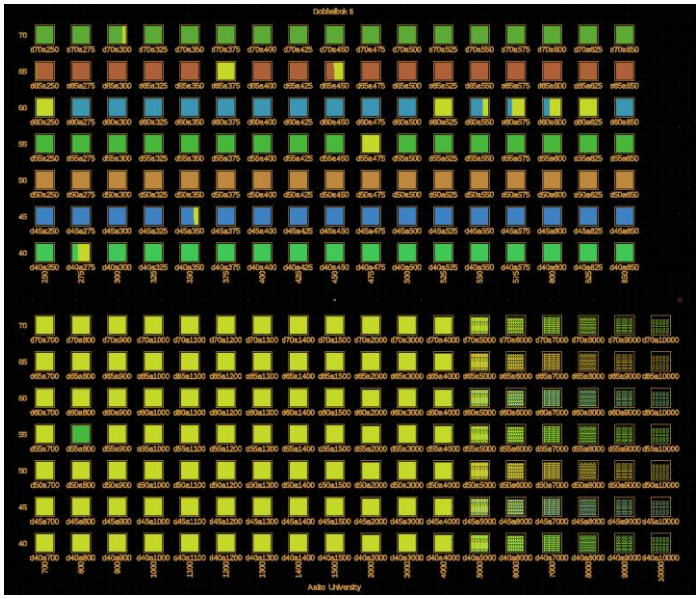

Figure 4.1. Pattern used for growing NWs. The marking indicates the NW seed diameter and distance between the nanowires. The inter-nanowire distance varies from 250 nm up to 10 μm.

4.2 Sample synthesis and characterization

4.2.1 Sample synthesis

GaAs NWs were fabricated with SAE using MOVPE system (Thomas Swan)[34]. The growth was performed on p-type GaAs (111) B substrates in atmospheric pressure. Prior to NW growth the growth templates were fabricated as follows. First, a 40-nm thick SiO_x layer was deposited using the plasma enhanced chemical vapor deposition (PECVD)

(Oxford Systems). Next, electron beam lithography (EBL) (Vistec) was performed to pattern the growth templates and reactive-ion etching (RIE) was used to transfer the patterns to the deposited SiO_x layer. Poly(methyl methacrylate) (PMMA) (MicroChem) was used as the EBL resist. The patterns contained triangular lattice arrays of circles with different diameters and pitches (Figure 4.1). Each array of circles was 100 µm by 100 µm in size and the diameter of the circles was varied from 40 nm up to 125 nm with a 5 nm step. The pitch was varied from 250 nm up to 10 µm with minimum step size of 50 nm. Prior to transferring the samples into the MOVPE reactor, resist stripping, degreasing and cleaning were performed in acetone, isopropanol and de-ionized water. The NW growth was performed using trimethylgallium (TMGa) and tertiary-butyl arsine (TBAs) as the precursors with H_2 carrier gas and total gas flow of 5 slm. The molar flows were 0.811 $\mu molmin^{-1}$ and 226.1 $\mu molmin^{-1}$ for TMGa and TBAs, respectively. The samples were thermally cleaned at 760°C under TBAs flow for 5 min just before initiating NW growth by turning TMGa flow on. The growth temperature was the same as for the thermal cleaning. Three samples were fabricated with different NW growth time. The growth times were 6 min, 11 min 30 s and 15 min. This was done to acquire approximately equal height for smaller and larger diameter NWs. When the growth was finished, the TMGa flow was cut off and the samples were cooled to 150°C under TBAs protection. A scanning electron microscopy (SEM) image of the samples with different nominal diameters (d) and pitches (a) has been shown in Figure 4.2.

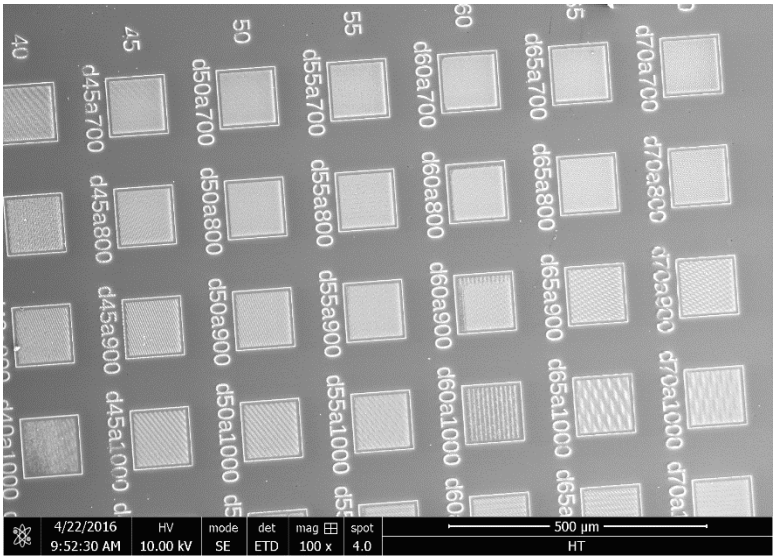

Figure 4.2. SEM image of the sample with different NW diameters and inter-nanowire distances. The lithographic diameter of the nanowires and inter-nanowire distances are denoted as d and a, respectively. Reprinted from Supplementary Information of Kargar, F. et al. Direct observation of confined acoustic phonon polarization branches in free-standing semiconductor nanowires. Nat. Commun. 7, 13400 (2016).

4.2.2 Sample characterization

Several sets of specially designed GaAs NWs with excellent surface quality and hexagonal cross section have been fabricated on top of a GaAs (111) substrate by selective-area epitaxy (SAE) utilizing metal-organic vapor phase epitaxy (MOVPE). The top facets of the NWs have the same crystallographic plane as the substrate while the side-facets are {110} planes. The NWs were grown in a perfect vertical arrangement in hexagonal arrays with the diameters ranging from 103 nm up to 135 nm. The important attributes of the samples were diameter uniformity within each batch (the relative standard deviation was about 3% for most tested NWs), large distance, *H*, between the NWs (we focused on the range from 700 nm to 3 μm; the smallest *H* was 250 nm while the largest was 10 μm), and

large length, *L*, of NWs (at least 10 times the NW diameter). Details of the sample fabrication and characterization are provided in **Table 4.1**. Scanning electron microscopy (SEM) image of the samples are shown in Figure 4.3 and Figure 4.4.

Table 4.1. Measurement of diameter and length of NWs based on SEM images

Diameter *D* (nm)	Relative Standard Deviation (%)	Length *L* (nm)	Relative Standard Deviation (%)
103	4.2	2058.6	4.8
111	5.7	1977.1	5.6
115	4.6	1716.5	4.4
122	2.9	1448.9	4.1
128	3.7	1277.3	3.3
135	1.7	1127.5	3.0

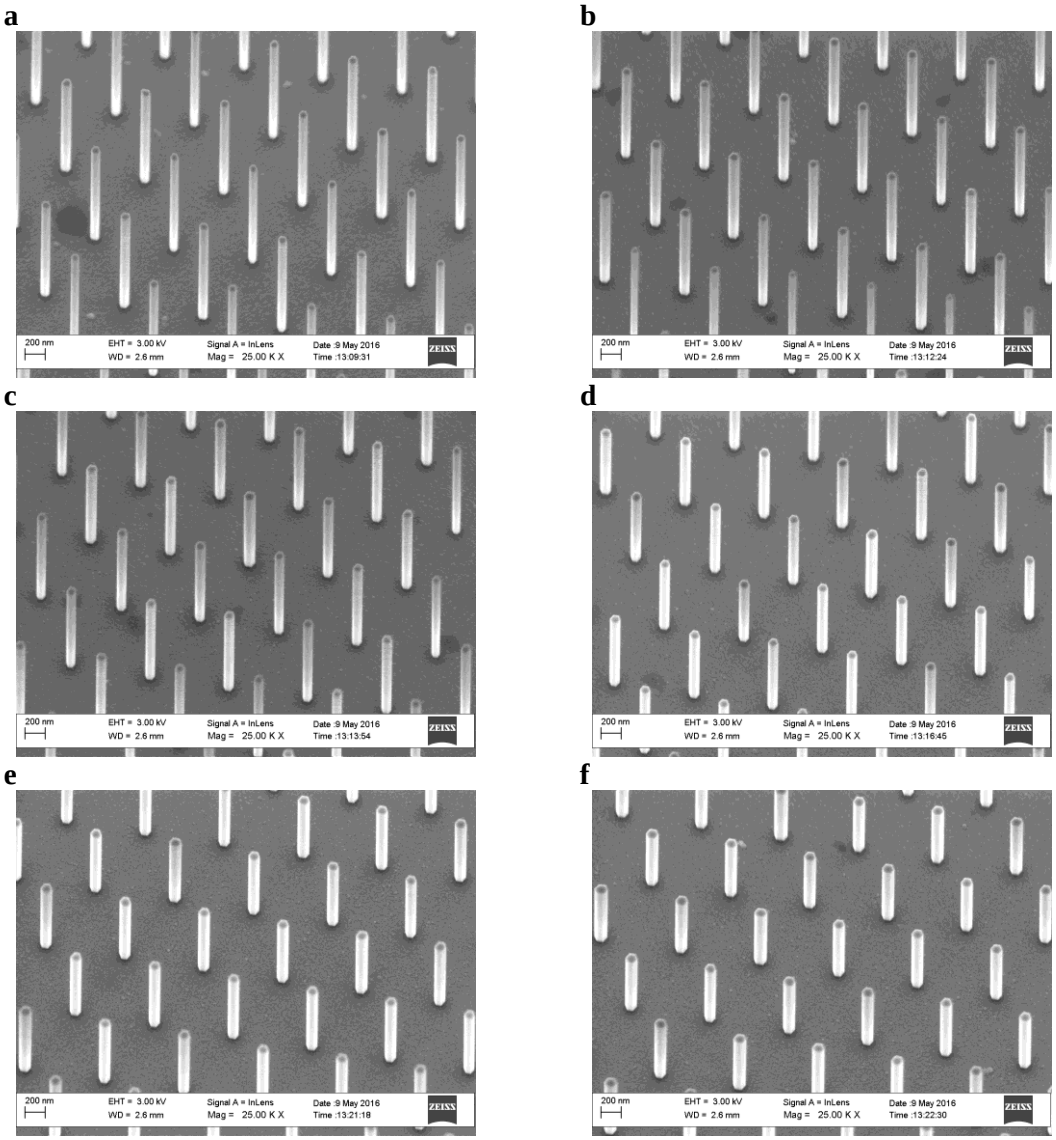

Figure 4.3. Side-view SEM images of samples. Detailed SEM analysis has been performed on all samples in order to determine the actual NW diameter, *D*, Length, *L* and distance, *H*, between the NWs. The representative data are for samples with the same *H*=800 nm and different diameter of (a) *D*=103 nm, (b) *D*=111 nm, (c) *D*=115 nm, (d) *D*=122 nm, (e) *D*=128 nm, and (f) *D*=135 nm. The ImageJ software was used to determine the length, *L*, and diameter of individual NWs. For each sample, more than 20 measurements were performed. The NW size data, including the standard deviation, are summarized in Table **4.1**.The results confirm the excellent quality and uniformity of the samples. Each batch contained NWs with almost the same diameter and length without significant variations. Reprinted from Supplementary Information of Kargar, F. et al. Direct observation of confined acoustic phonon polarization branches in free-standing semiconductor nanowires. Nat. Commun. 7, 13400 (2016).

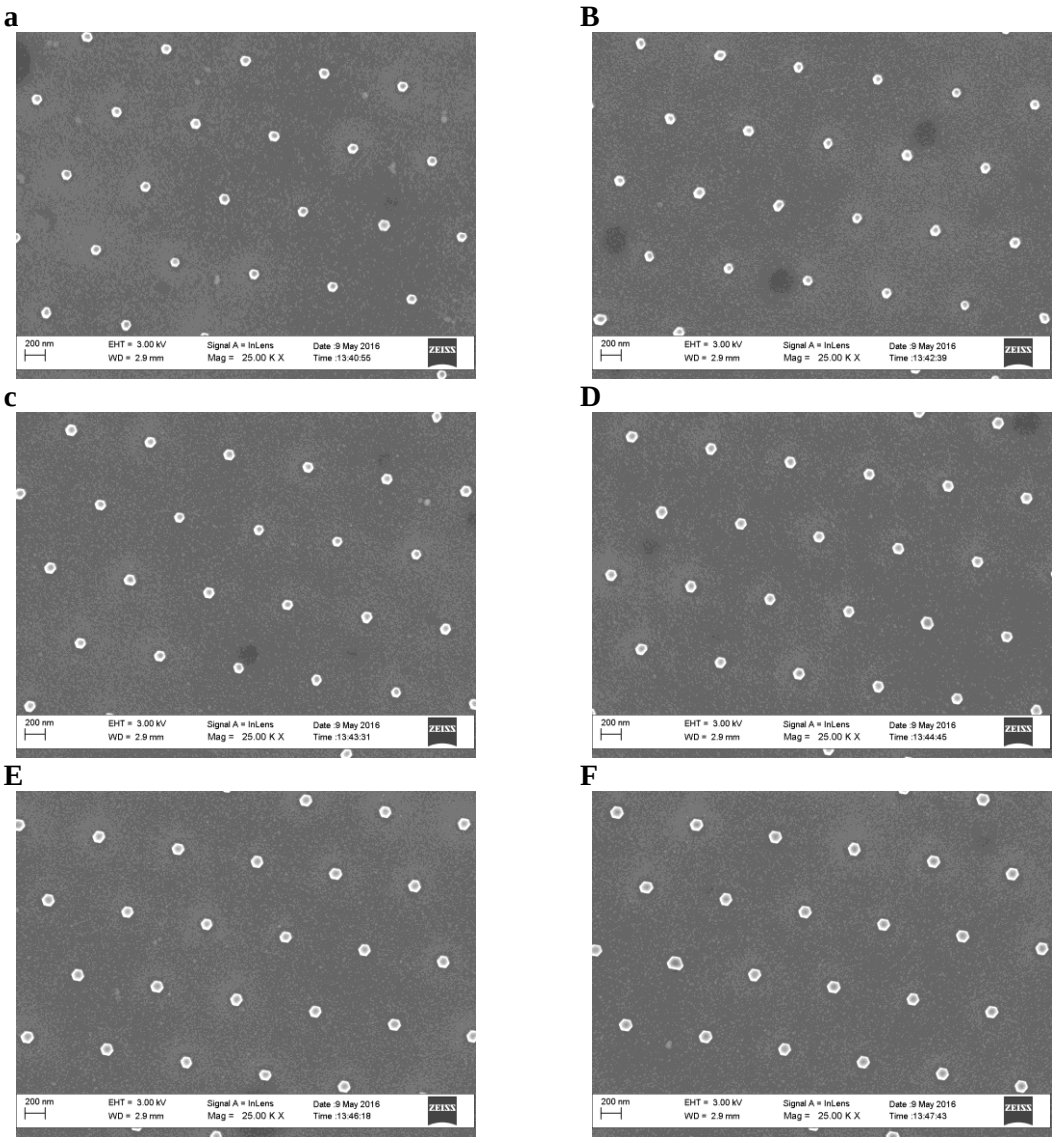

Figure 4.4. Top-view SEM images of samples. Detailed SEM analysis has been performed on all samples in order to determine the actual NW diameter, *D* and distance, *H*, between the NWs. The representative data are for samples with the same *H*=800 nm and different diameter of (a) *D*=103 nm, (b) *D*=111 nm, (c) *D*=115 nm, (d) *D*=122 nm, (e) *D*=128 nm, and (f) *D*=135 nm. Reprinted from Supplementary Information of Kargar, F. et al. Direct observation of confined acoustic phonon polarization branches in free-standing semiconductor nanowires. Nat. Commun. 7, 13400 (2016).

4.3 Brillouin-Mandelstam spectroscopy

4.3.1 Methods

The experiments were carried out in backscattering geometry with p-polarized incident light using a solid-state diode pumped laser operating at λ=532 nm. The laser light was focused on the samples through a lens with *NA*=1.4. The scattered light was collected with the same lens and directed to the high-resolution six-pass tandem Fabry-Perot interferometer (JRS Instruments). A specially designed stage allowed to rotate the samples up to 60^{o} relative to the direction of the incident laser light with an accuracy of 0.02^{o}.

4.3.2 Measurements

We used Brillouin-Mandelstam light scattering (BMS) spectroscopy as a tool to measure the dispersion of acoustic phonons with energies in the range from 2 GHz up to 200 GHz near the Brillouin zone (BZ) center. Various modifications of Brillouin spectroscopy[35,36] are gaining popularity for investigating acoustic phonon and magnon energies in phononic crystals and other materials[31,37–46]. Changing the angle of light incidence with respect to the substrate allowed us to vary the probing phonon wave-vector, *q*, and determine the dispersion near the BZ center. An SEM image of the samples as well as the schematic of the experiment is shown in Figure 4.5 (a-b). The large inter-NW distance *H*, which was much larger than the laser wavelength, λ, ensured that NWs scatter light individually, e.g. neither light interference nor elastic coupling via the substrate affect the results. We used the samples with *H* up to 3 μm to verify that the measured spectral

characteristics are independent of *H*. Large *H* and *L>>D* also ensure that each NW can be modeled theoretically as an infinite NW with free-surface boundaries. These unique characteristics of NW samples made possible investigation of the phonon spectrum features originating in individual NWs.

There are three mechanisms, which contribute to light scattering in our samples. They are scattering from the bulk, i.e. the volume of the substrate via the elasto-optic mechanism[35,36]; from the surface of the substrate via the surface ripple mechanism[35,36]; and from the side-facets of NWs via the surface ripple mechanism as well. In the volumetric mechanism (i) the phonon wave vector, *q*, is fixed at $q_B = 4\pi n/\lambda$ where *n* is the refractive index of GaAs. In the ripple scattering mechanisms (ii) and (iii), the phonon wave vector is given by $q_{S-S} = (4\pi/\lambda)\sin(\alpha)$ for the substrate and $q_{S-NW} = (4\pi/\lambda)\cos(\alpha)$ for NWs (see notation for angle α in Figure 4.5 (b)). The difference in the angle dependence is due to the perpendicular alignment of NWs. In probing the ripple scattering mechanism, changing α allows one to vary *q* within a certain range. The volumetric elasto-optic scattering is absent in our NWs because $D < \lambda$. Although the light scattering is from the NW surface ripples it inherently depends on the confined phonon modes inside the NW, which create the ripples. In our experiments, changing α from 15° to 40° corresponded to 6.1 $\mu m^{-1} \leq q_{S-S} \leq 15.2\ \mu m^{-1}$ and 18.1 $\mu m^{-1} \leq q_{S-NW} \leq 22.8\ \mu m^{-1}$ in the ripple scattering from the substrate and NWs, respectively. Taking into account that n=4.13 for GaAs[47] at λ=532 nm the *q* value for the substrate elasto-optic scattering was fixed at q_B=97.6 μm^{-1}.

Figure 4.5 (c) shows BMS spectra of NWs with the diameter D=122 nm (inter-NW distance H=800 nm) extracted from SEM data, and the substrate without NWs in the frequency range from 20 GHz to 125 GHz. The phonon peaks at 45.6 GHz and 85.8 GHz in the spectrum from the substrate correspond to the transverse acoustic (TA) and longitudinal acoustic (LA) polarization branches. These peaks originate from the true acoustic bulk phonons that have zero frequency at the BZ center, i.e. $\omega(q=0)=0$. The bulk phonon peaks are present in the spectra of NW samples as well because part of the signal is coming from the substrate. The most interesting feature of NW spectrum is the appearance of additional peaks attributed to the confined acoustic (CA) phonons. These phonons are quasi-optical in nature, in a sense, that their energy is non-zero at the BZ center, i.e. $\omega(q=0)\neq 0$. All confined phonons in NWs are hybrid in nature comprising of vibrations with different polarization. Although confined phonons are higher in energy than the true acoustic phonons, in the experimental spectrum, they appear at smaller frequencies because the probing phonon wave vectors are different: $q_{S-NW} < q_B$. Figure 4.5 (d) presents the evolution of the BMS spectrum for the same NW sample for different values of q that are varied by changing the angle α. We were able to resolve six confined phonon branches denoted as CA_i (i is the confined phonon index). For clarity, the BMS spectra for the bare substrate without nanowires at various incident light angles has been shown in Figure 4.6. The peak below 15 GHz is a mixture of the true LA phonons in the substrate and LA-like phonons in NWs.

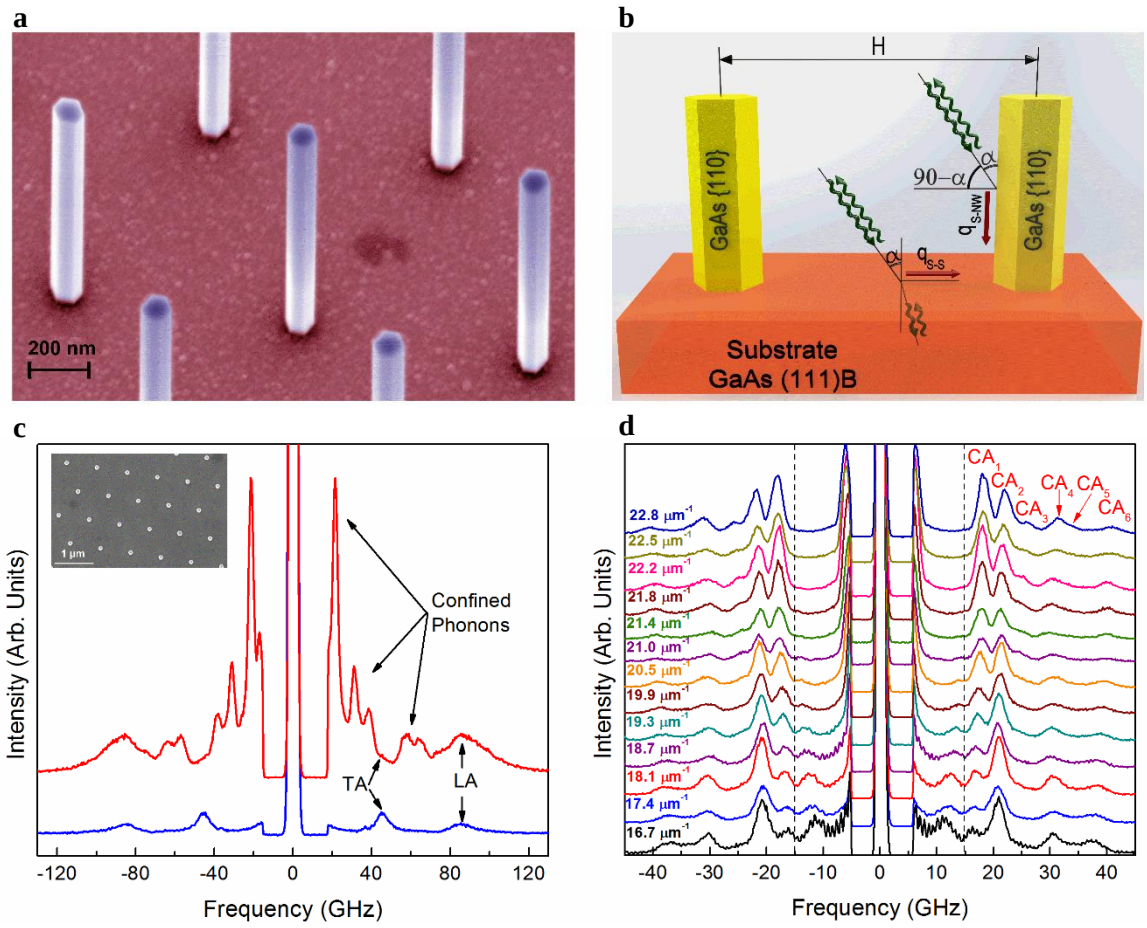

Figure 4.5. Free-standing GaAs nanowires and their acoustic phonon spectrum. (a) SEM image of NWs showing their diameter uniformity, orientation and large inter-nanowire distances (reaching up to H=3.0 μm in some samples). The pseudo-colors are used for clarity. (b) The schematic of the BMS experiment with notation for the substrate angle of incident α, which translates to $\pi/2$-α for NWs. Two mechanisms of light scattering – elasto-optic inside the substrate and ripple scattering from the side-facets of NWs and substrate surface – are illustrated with green arrows. (c) Measured phonon spectrum for NWs with the diameter D=122 nm (red curve) and a substrate without NWs (blue curve). The inset shows a top-view SEM image of a representative NW sample. The regular LA and TA phonon peaks are present in both spectra. Additional peaks in the NW spectrum correspond to the confined acoustic phonons in individual NWs visible via the ripple scattering mechanism. These peaks appear at lower frequency than bulk phonons owing to the difference in the probing phonon wave vector q. (d) Evolution of the spectrum with the changing probing phonon wave vector defined by α. The confined phonon branches are denoted as CA_1, CA_2, etc. Dash-lines are used to separate the peaks attributes to CA_i modes from the ones corresponding to NW's LA-like polarization branch for clarity. The spectral position of the peaks was accurately determined by the Lorentzian fitting.

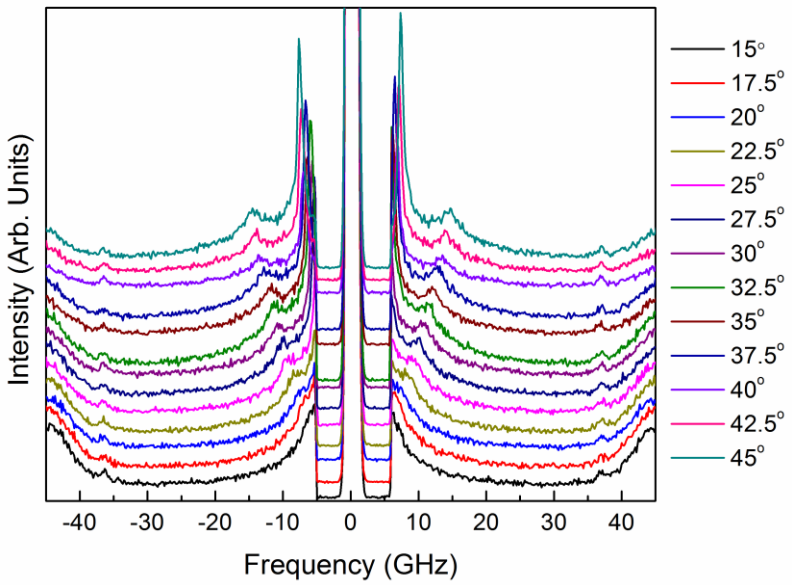

Figure 4.6. BMS spectrum of the reference substrate. In order to be able to distinguish and exclude, if needed, the effect of the substrate, BMS has been conducted at different incident angles on a reference substrate without NWs. As it can be seen, as the incident angle increases, the small peak which originates from the surface ripple scattering of the substrates surface moves to higher energies. At incident angles of ~40° or higher, this peak mixes with the true LA mode of the NWs and makes the spectrum noisy. At incident angles close to this value, another sharp peak appears at ~5 GHz which corresponds to GaAs surface Rayleigh wave. The angles for the study of NWs were selected to minimize the substrate effects and facilitate the data analysis. Reprinted from Supplementary Information of Kargar, F. et al. Direct observation of confined acoustic phonon polarization branches in free-standing semiconductor nanowires. Nat. Commun. 7, 13400 (2016).

4.4 Theoretical simulations

4.4.1 Finite-element method simulations

The phonon dispersion and displacement patterns have been calculated in the elastic continuum approximation using FEM implemented in COMSOL Multiphysics package. The GaAs sample is assumed to have zinc-blende (ZB) crystal structure. The out-of-plane direction of the nanowire is along *x*, which is also the growth direction (*i.e.* [111]). From

the second-order continuum elastic theory, the equation of motion for the elastic vibration is

$$\rho\left(\partial^2 u(\mathbf{r})/\partial t^2\right)=\partial S(\mathbf{r})/\partial x_i \tag{4.1}$$

Here u(**r**) is the three-component displacement vector at coordinate **r**; ρ is the mass density; S(**r**) is stress tensor that can be constructed from displacement by $S_{ij} = C_{ijkl}\,\varepsilon_{kl}$ with the six-component elastic strain tensor[48], $\varepsilon(\mathbf{r})=\frac{1}{2}[(\nabla\mathbf{u})^{T}+(\nabla\mathbf{u})]$. The fourth-ranked elastic stiffness tensor, C_{ijkl}, is also expressed in the non-tensor notation as C_{ij} with indices *i, j, k, l* running over the spatial coordinates (*x, y, z*). The elastic constants, C_{ij}, used in simulation correspond to GaAs in [001] direction: C_{11}=118.8 GPa, C_{12}=53.8 GPa, C_{44}=59.4 GPa[48]. According to *ab initio* simulations[49] and experiment[49], the bulk stiffness tensor is equally applicable to nanowire geometry as long as the nanowire diameter is not smaller than 20 nm. In order to take into account the growth direction of the nanowire we applied the tensor rotation operation to transform the stiffness matrix in [111]-oriented coordinate system as

$$C_{ijkl}^{[111]} = \Sigma_{\alpha\beta\gamma\delta} U_{i\alpha} U_{j\beta} U_{k\gamma} U_{l\delta} C_{\alpha\beta\gamma\delta}^{[001]} \tag{4.2}$$

Here *U* is the rotational matrix for the Euler angles. The transformed elastic matrix and material parameters are summarized in **Table 4.2**. The simulation geometry is discretized using finite element scheme to obtain the solution of the elasticity equation in the frequency domain as- $\rho\omega^2 u=\nabla.\mathbf{S}$, where ω is the Eigen frequency. The free surface

boundary conditions are applied at all outer facets in the radial direction by setting $\varepsilon_{ij}n_j=0$, where n_j is the outward normal unit-vector.

Table 4.2. Material parameters								
C_{11} (GPa)	C_{12} (GPa)	C_{13} (GPa)	C_{15}=-C_{25}=-C_{46} (GPa)	C_{33} (GPa)	C_{44} (GPa)	C_{66} (GPa)	ρ (kgm^{-3})	ε_r
145.7	44.8	35.8	12.7	154.6	41.5	50.4	5317	13.18

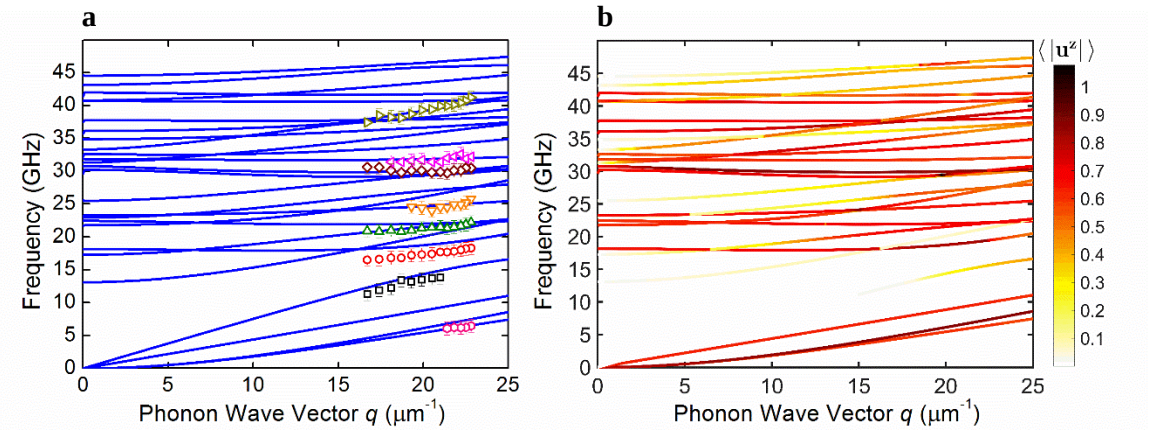

Figure 4.7. Confined acoustic phonon dispersion in semiconductor nanowires. (a) Measured and calculated phonon dispersion for a GaAs nanowire along [111] direction. The experimental data points, indicated with symbols and error bars, were obtained for NWs with the diameter D=122 nm determined from SEM inspection. Experimental uncertainties, on the order of 1 GHz, is within the standard deviation of the NW diameters (b) Calculated dispersion with the color indicating the average surface displacement of the NW side-facet ($\langle|\mathbf{u}^z|\rangle$) perpendicular to the phonon $q_{S\text{-}NW}$. Darker color corresponds to higher phonon mode activity in light scattering.

4.5 Results

To understand and confirm the confined nature of the observed phonon peaks above 15 GHz, we solved the elasticity equation for NWs using the finite-element method. The simulations were carried out for NWs with hexagonal cross-sections using GaAs elastic constants for a specific crystallographic direction ([111]) and NW diameter determined

from SEM. Figure 4.7 (a) shows the simulated phonon dispersion (solid curves) in a hexagonal NW along the [111] direction for *D*=122 nm. One can see excellent agreement between the experimental data and modeling results for both true acoustic and confined phonon branches. The accurate BMS peak positions were determined using Lorentzian fitting (Figure 4.8). Experimental uncertainties, on the order of 1 GHz, is within the standard deviation of the NW diameters (i.e., 2.9% for *D*=122 nm). Other sources of uncertainty are inevitable variations in the elastic behavior of NWs resulting from the stacking faults and possible small inclusions of the wurtzite (WZ) phase to the dominant zinc-blende (ZB) polytype in NWs with various diameters. This may result in a small change in the LA-like sound velocity $\upsilon_s = (C_{11}/\rho)^{1/2}$, defined by the slope of this branch. Additional analysis of the model sensitivity to parameter variations is provided in Figure 4.9 and Figure 4.10.

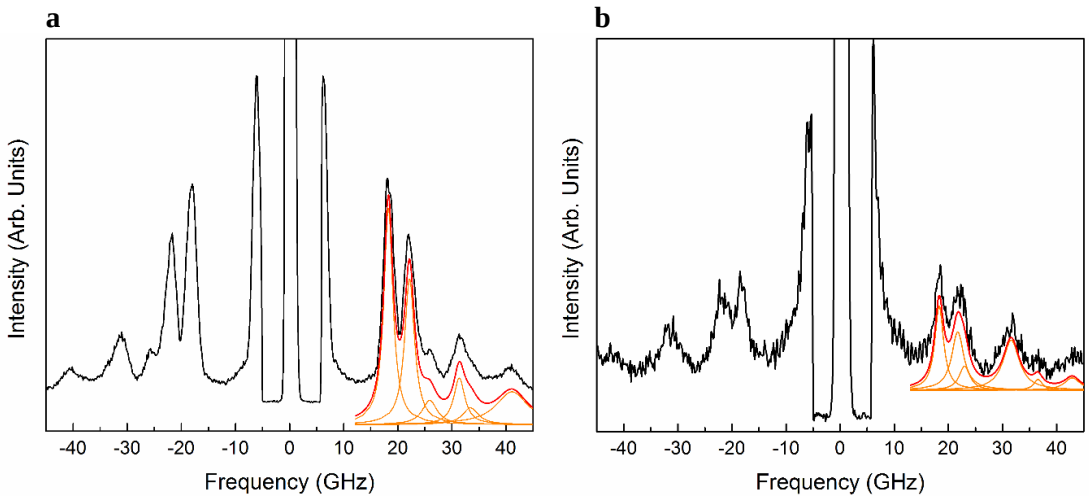

Figure 4.8. Examples of BMS spectrum analysis. An example of peak deconvolution for BMS results of NWs with diameter D=122 nm and inter-nanowire distance (a) H=800 nm and (b) H=3000 nm is presented for constant phonon wave-vector of $q_{S\text{-}NW}$=22.8 μm^{-1}. In most of cases, the measured confined phonon and true acoustic phonon peaks were clearly observed. They could be fitted with individual Lorentzian functions. However, some peaks were too close to each other to be visually resolved. In these cases, peak deconvolution with several Lorentzian functions was used. The positions of the Lorentzian functions were then checked using the calculated phonon dispersion. As one can see, increasing the inter-NW distance does not change the position of the peaks. The signal-to-noise ratio decreases (fewer NWs are illuminated) making fitting less accurate. The date proves that NWs scatter light individually. For both spectra, while the first two peaks are very sharp the peak at ~35 GHz is broad. For the broad peak, a standard deconvolution procedure has been used. One can see that the broad peak consists of two elemental peaks close to each other. The orange lines in this figure are single Lorentzian functions while the red line represents the cumulative fitting. The positions of the elemental Lorentzian functions used in the decomposition are in excellent agreement with the calculated dispersion. Reprinted from Supplementary Information of Kargar, F. et al. Direct observation of confined acoustic phonon polarization branches in free-standing semiconductor nanowires. Nat. Commun. 7, 13400 (2016).

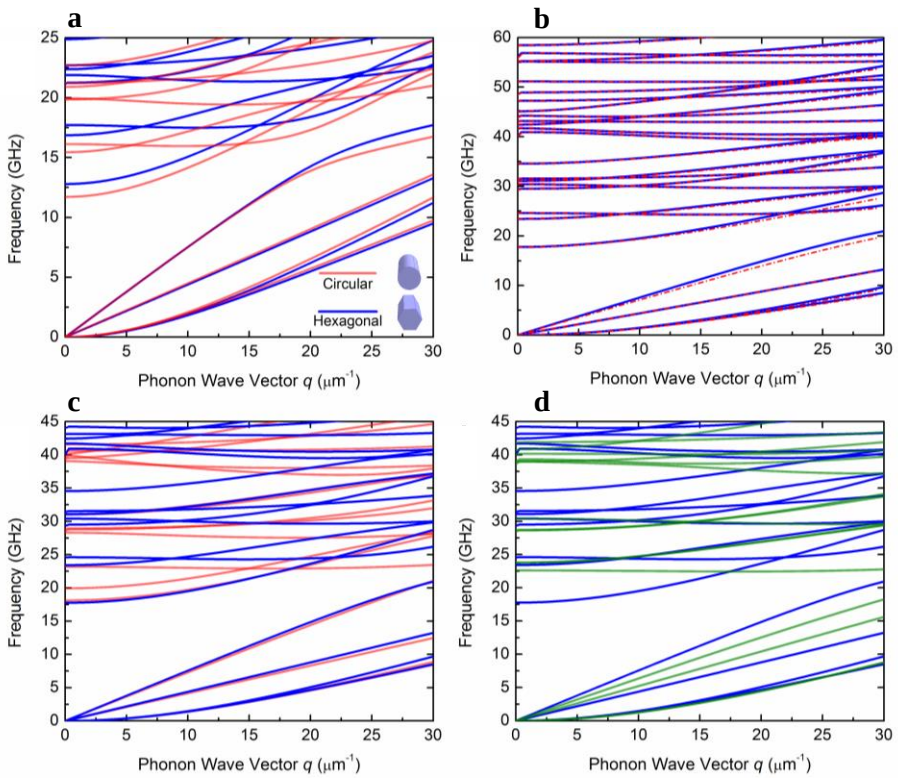

Figure 4.9. Effect of different parameters on calculated phonon dispersion of NWs. (a) Sensitivity of the phonon dispersion to the NW cross-section shape. The red and blue curves correspond to the circular and hexagonal cross-section, correspondingly. The data were calculated for NW diameter D=125 nm and crystal orientation along [111]. One can see that depending on the NW cross-section shape the confined phonon modes can deviate by ~1.5 GHz to 2 GHz, which can be resolved experimentally. (b) Effect of stiffness coefficient (matrix element C_{11}) on phonon dispersion. The longitudinal acoustic (LA) sound velocity may vary slightly from sample to sample due to growth condition and residual strain. This can be reflected in numerical modeling via changes in the C_{11} value. One can see that tuning C_{11} by 10% affects slightly the LA-like mode but does not change the BMS active confined acoustic (CA) mode. This is in line with our experimental observation that the BMS peaks of confined mode frequencies remain same for different sample with fixed D and cross-section. (c) Sensitivity of the phonon dispersion to crystalline structure by simulating it for zinc-blende (ZB) (blue curve) and wurtzite (WZ) (red curve) phases of NW with D=90 nm. (d) Influence of the crystal orientation on the phonon dispersion in ZB GaAs NW with D=90 nm. Changing orientation reduces the original point group symmetry. This results in the breaking of degeneracy in FA modes (lowest two branches). The group velocity of LA-like branch also depends strongly on crystal orientation. This explains why the data on crystal orientation of NW samples were important for interpretation of the experimental data. The blue and green curves represent the data for zinc-blende [111] and zinc-blende [001] directions, respectively. Reprinted from Supplementary Information of Kargar, F. et al. Direct observation of confined acoustic phonon polarization branches in free-standing semiconductor nanowires. Nat. Commun. 7, 13400 (2016).

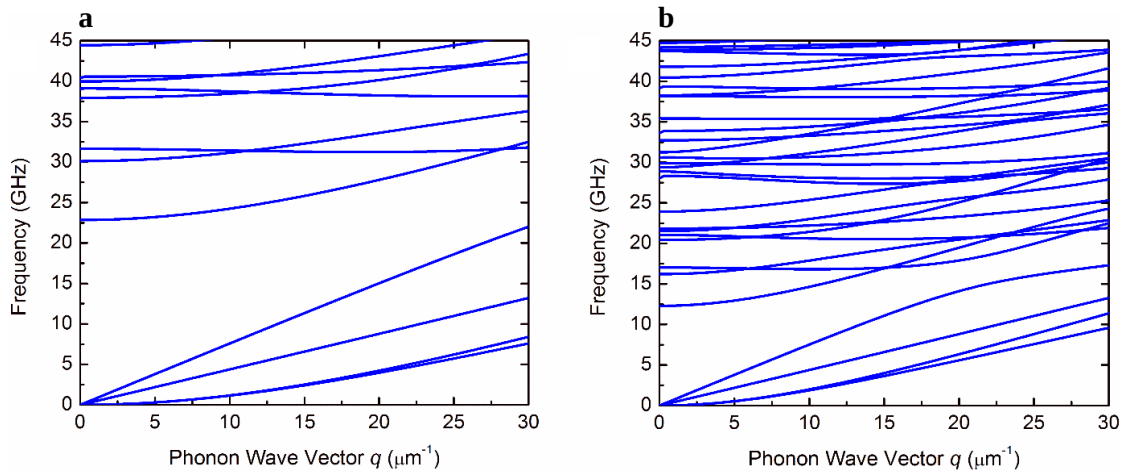

Figure 4.10. Calculated phonon dispersion for NWs with different diameters. A comparison of phonon dispersion of GaAs NW along [111] direction for different diameter (a) D = 70 nm and (b) D = 130 nm is presented. At small values of q<15 μm^{-1}, the fourth phonon branch is LA-like and demonstrates sufficiently high group velocity. The increase of q leads to the confinement induce changes in polarization (the phonon modes become mixture of LA and TA vibrations) with the corresponding decrease in its group velocity. Reprinted from Supplementary Information of Kargar, F. et al. Direct observation of confined acoustic phonon polarization branches in free-standing semiconductor nanowires. Nat. Commun. 7, 13400 (2016).

4.6 Discussion

Our proof of the confined nature of the phonons is based on excellent agreement of the dispersions obtained from BMS experiments and calculated for the exact NW shape and material parameters. In order to confirm that the identified phonon modes are Brillouin active, we calculated the average surface displacement of NW's side-facet perpendicular to q_{S-NW}. In the surface scattering mechanism, the phonon modes that produce displacement perpendicular to q_{S-NW} in the plane of scattering are those likely to contribute to the BMS spectrum. The scattering cross-section is given by[50]

$$d^2\sigma/d\Omega\, d\omega_s = \left(\zeta\ \omega_I^4/16\pi^2 c^4\right) F^2 \left\langle \left|u^z(0)\right|^2 \right\rangle_{q_x,\omega} \tag{4.3}$$

Here ζ is a coefficient proportional to the illuminated area, ω_I is the frequency of the incident light, c is the speed of light in the vacuum, F is a function of the incident and scattered light angles as well as n of the scattering medium. The last term <…> is the surface-displacement power spectrum with q_x projection to the surface. The calculated displacements, which enter Eq. (4.3), are shown in Figure 4.7 (b) by the color of the simulated phonon branches. The results are in agreement with the experiment in a sense that the measured data points are all within the Brillouin active segments of the polarization branches. The fact that these branches are active is in line with the observation that the considered phonon modes are hybrid in nature.

The phonon modes are visualized in Figure 4.11 (a) and (b) as the normalized displacement field distributions in NWs for two wave-vectors q_{S-NW} =0.3 μm^{-1} and q_{S-NW} =18.0 μm^{-1} – close and away from the BZ center, correspondingly. The modes become more hybrid in nature as q increases. The active modes show strong surface ripple on the side facets of NWs. The symmetry of the confined modes is complicated. The point group of ZB is T_d with 24 invariant operations whereas WZ is characterized by C_{6v} [ref. 49]. Confined NW geometry reduces the symmetry to C_{3v}. The two lowest branches are flexural acoustic (FA) modes of E_1 symmetry with the quadratic dispersion $\omega \propto k^2$. The degeneracy of this branch is broken for NWs along the [111] direction. The next two acoustic modes, torsional acoustic of A_2 symmetry and LA-like of A_1 symmetry, respectively, have linear

dispersion $\omega \propto k$, near the BZ center. The confined branches mainly belong to the higher symmetry groups e.g. E_2, B_1, B_2.

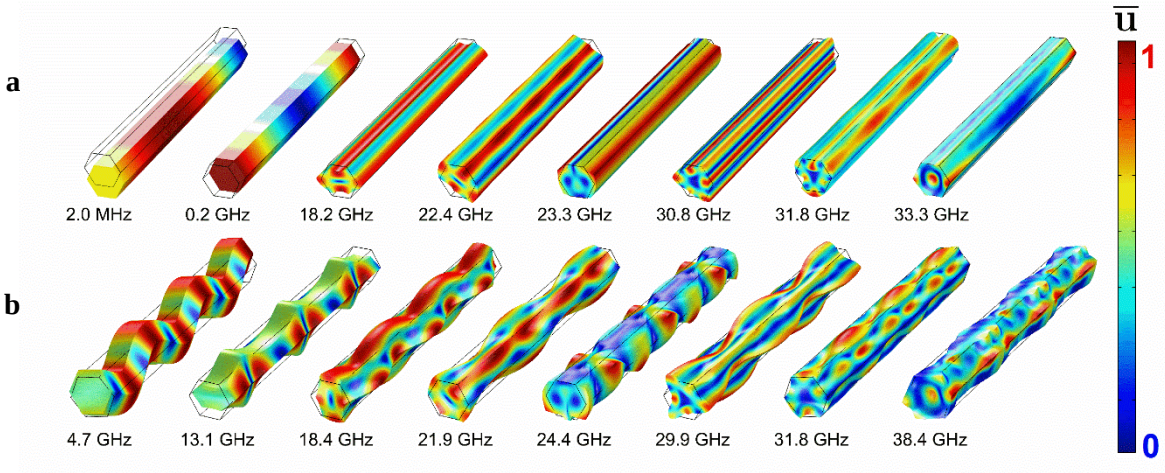

Figure 4.11. Normalized displacement field of the Brillouin-active phonon modes. The calculated data are for a 1-μm long NW with (a) $q_{S\text{-}NW}$ = 0.3 μm^{-1} and (b) $q_{S\text{-}NW}$ = 18.0 μm^{-1}. The red color corresponds to stronger displacement.

The final element of evidence of spatial confinement of acoustic phonons in free-standing NWs comes from the analysis of the diameter dependence of the CA phonon frequencies (energies). Figure 4.12 (a) shows the measured phonon spectra for different NW diameters, D (H=800 nm for all samples). One can see that with increasing D, the frequencies of the confined phonons decrease. The trend and the magnitude of the frequency change are consistent with the theory (see calculated dispersions for various D in the Figure 4.10). In Figure 4.12 (b), we present spectra of NWs with the constant D=122 nm and varying H. The spectral position of CA peaks does not depend on the inter-NW distance. The absence of H dependence indicates that the measured spectral features are characteristics of individual NWs. There is no elastic coupling among NWs. The spatial

phonon confinement in the free-surface NWs is distinctively different from the phonon spectrum changes owing to the periodic boundary conditions in the phonon band-gap materials.

A remaining intriguing question in confirming the confined nature of CA peaks is why their full-width-at-half-maximum (FWHM) appear smaller than that of the substrate LA phonon peak (see Figure 4.5 (c)). Theory suggests that the phonons with smaller group velocity, υ_G, should be more strongly scattered[18]. The phonon life-time limited by the point-defect scattering, $\tau_D = (4\pi\upsilon_G^3)/(V_o\omega^4\Gamma)$, rapidly decreases with decreasing υ_G (here V_o is the volume per atom and Γ is the defect scattering factor). The Umklapp limited phonon life-time also decreases with decreasing υ_G. The answer to this question is that FWHM of the elasto-optic and ripple mechanism peaks cannot be compared directly. The FWHM of the LA peak from the substrate ($\Delta\omega$ = 13.6 GHz) is defined by the light absorption. For an opaque crystal with the refractive index $n = n_1 + in_2$, theoretical broadening for the elasto-optic scattering[51] is $\Delta\omega/\omega = 2n_2/n_1$. Using for GaAs, n_1=4.13 and n_2=0.34 [ref. 47], we obtain $\Delta\omega/\omega$ = 0.164, which closely matches with the measured $\Delta\omega/\omega$ = 0.158. For the CA phonons, observed in our experiments via the surface ripple scattering, the peak broadening is defined by the aperture effects[35,36].

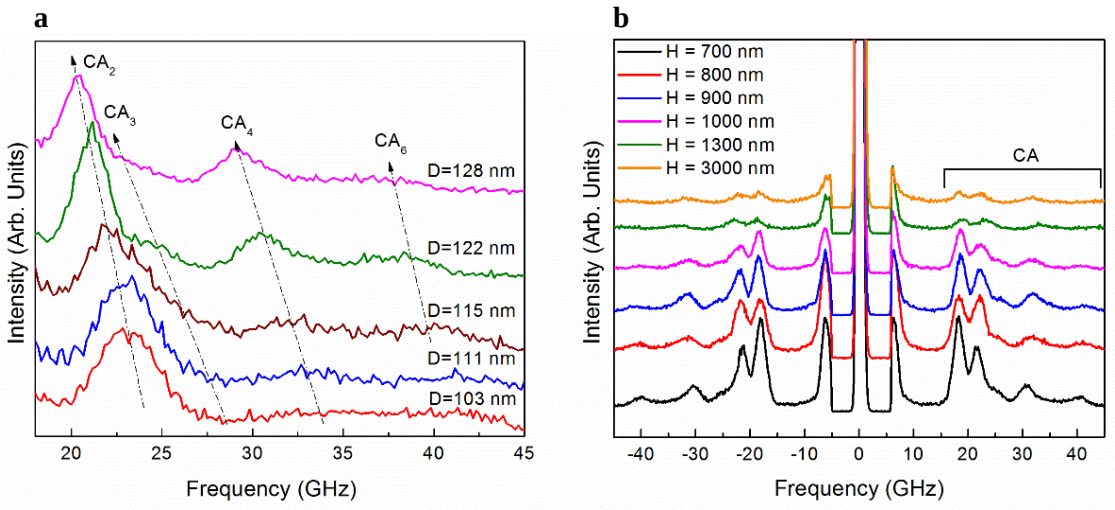

Figure 4.12. Effect of the diameter and inter-nanowire distance on confined phonon energies in nanowires. (a) Brillouin-Mandelstam spectrum for NWs with different diameter at a constant probing phonon wave vector $q_{S\text{-}NW}$ =18.1 μm^{-1}. The decrease in the frequency of the confined phonons with increasing NW diameter is clearly visible. The confined phonon branches show strong diameter dependence even for relatively large *D* values in the range from 103 nm to 128 nm. The diameter dependence proves conclusively the presence of the spatial confinement effects at the length scale above the grey phonon mean-free path. (b) Measured spectrum for a set of NWs with the constant diameter *D* = 122 nm and varying inter-NW distance *H* at a constant probing phonon wave vector $q_{S\text{-}NW}$ =22.8 μm^{-1}. The data are presented for the same fixed accumulation time of 30 minutes. The spectral position of the CA peaks does not depend on *H*. The intensity decreases with increasing *H* owing to smaller number of illuminated NWs. The absence of the inter-NW distance dependence proves that the observed spectral features are characteristics of individual NWs.

The fact that the acoustic phonon spectrum becomes strongly modified near BZ center at the length-scale much larger than the grey phonon MFP or the thermal phonon wavelength has important implications. It means that the acoustic phonon confinement can affect the electron – phonon scattering rates[52] in the structures comparable in size to the state-of-the-art electronic devices. The BZ-center phonons (q<10^6 cm^{-1}) are essential for controlling electron relaxation[2,15,17,23]. The frequency-dependent average phonon group velocity[53] $\langle \upsilon(\omega) \rangle = g(\omega) / \Sigma_j 1/\upsilon_j(\omega)$, which affects the heat conduction, also changes (here

$g(\omega)$ is the number of phonon branches in the spectra with the frequency ω, and $\upsilon_j(\omega)$ is the group velocity of the phonon mode of the subband *j* and frequency ω. The group velocity of each phonon branches is shown in Figure 4.13 (a). In NWs with *D*~100 nm, $\langle\upsilon(\omega)\rangle$ drops to less than half of the LA-like mode sound velocity in the frequency range around 20 GHz – 60 GHz due to emergence of the confined phonon branches.

Our measurements were conducted in the GHz range of phonon frequencies, which dominates heat conduction at low temperature[54]. The fact that we established the existence of the confined phonon branches at RT indicates that the effects can be even stronger at low temperature. THz phonons are considered to be the main contributors to thermal transport at RT owing to a much higher DOS, which scales as ω^2 in bulk crystals. However, the nearly dispersion-less confined phonons in the BZ-center can substantially change the DOS (Figure 4.13 (b)) resulting in a greater role for the GHz phonons in thermal transport. Even in bulk, the low-frequency phonons, including the GHz range, participate in the phonon – phonon scattering processes[1,55]. The role of the low-frequency phonons is greatly increased in alloyed materials because the higher frequency phonons scatter more strongly[56]. A possibility of reducing the phonon thermal conductivity in nanostructures with smooth boundaries is important for thermoelectric devices. The phonon confinement mechanism allows one to reduce the thermal conductivity without degrading the electron transport. This may become particularly relevant in the quest for efficient low-temperature thermoelectric materials.

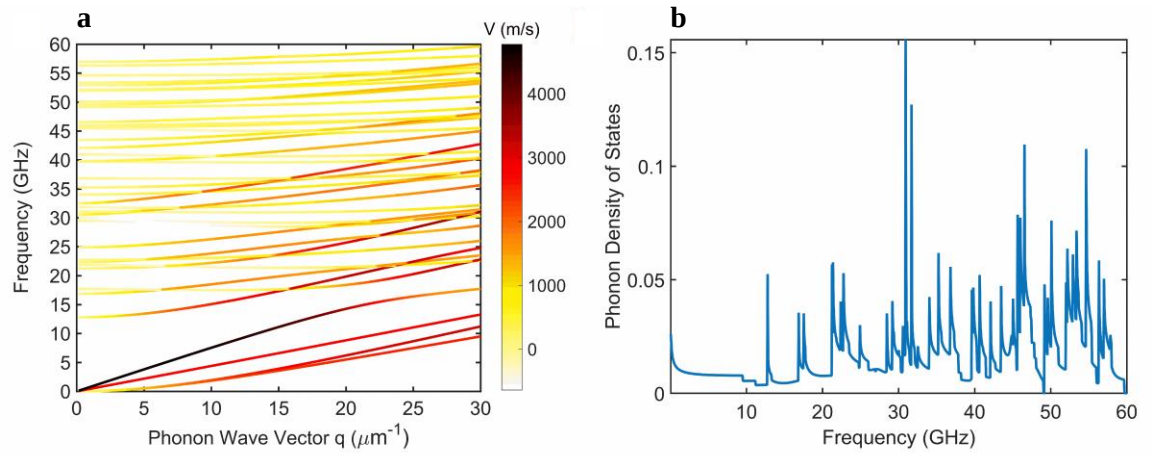

Figure 4.13. Calculated phonon group velocity and density of states. (a) Calculated phonon dispersion indicating the relative contribution of each branch to the mode-averaged phonon group velocity. The change in the color from yellow to black corresponds to increasing contribution to the mode-average phonon group velocity. (b) Calculated phonon density of states. The simulations were performed for D = 122 nm. The data indicates that the effect of the confined phonons is significant, leading to reduction of the average group velocity. The phonon density of states is modified as compared to bulk owing to the emergence of the confined phonon bands. Reprinted from supplementary Information of Kargar, F. et al. Direct observation of confined acoustic phonon polarization branches in free-standing semiconductor nanowires. Nat. Commun. 7, 13400 (2016).

4.7 Conclusions

In summary, we conducted study of confined acoustic phonon modes in GaAs nanowires and reported up to ten confined acoustic phonon polarization branches in nanowires with a diameter as large as 128 nm which is an order of magnitude larger that grey mean free path in this material. In addition, we carried out finite-element simulations for obtaining the phonon dispersion in nanowires and demonstrated an excellent agreement between experimental and theoretical results. The phonon confinement effects result in a decrease in the phonon group velocity along the nanowire axis and changes in the phonon

density of states. The obtained results can lead to more efficient nanoscale control of acoustic phonons, with benefits for nanoelectronic, thermoelectric and spintronic devices.

References

1. Srivastava, G. P. *The physics of phonons*. (CRC Press, 1990).

2. Stroscio, M. A. & Dutta, M. *Phonons in nanostructures*. (Cambridge University Press, 2001).

3. Antonelli, G. A., Maris, H. J., Malhotra, S. G. & Harper, J. M. E. Picosecond ultrasonics study of the vibrational modes of a nanostructure. *J. Appl. Phys.* **91,** 3261–3267 (2002).

4. Lu, M.-H., Feng, L. & Chen, Y.-F. Phononic crystals and acoustic metamaterials. *Mater. Today* **12,** 34–42 (2009).

5. Cheng, W., Wang, J., Jonas, U., Fytas, G. & Stefanou, N. Observation and tuning of hypersonic bandgaps in colloidal crystals. *Nat. Mater.* **5,** 830–836 (2006).

6. Eichenfield, M., Chan, J., Camacho, R. M., Vahala, K. J. & Painter, O. Optomechanical crystals. *Nature* **462,** 78–82 (2009).

7. Liu, Z. *et al.* Locally resonant sonic materials. *Science (80-.).* **289,** 1734–1736 (2000).

8. Vasseur, J. O. *et al.* Experimental and theoretical evidence for the existence of absolute acoustic band gaps in two-dimensional solid phononic crystals. *Phys. Rev. Lett.* **86,** 3012 (2001).

9. Ghosh, S. *et al.* Dimensional crossover of thermal transport in few-layer graphene. *Nat. Mater.* **9,** 555–558 (2010).

10. Balandin, A. A. & Nika, D. L. Phononics in low-dimensional materials. *Mater. Today* **15,** 266–275 (2012).

11. Volz, S. *et al.* Nanophononics: state of the art and perspectives. *Eur. Phys. J. B* **89,** 1–20 (2016).

12. Bandyopadhyay, S. *Physics of Nanostructured Solid State Devices*. (Springer Science & Business Media, 2012).

13. Bandyopadhyay, S. & Cahay, M. *Introduction to spintronics*. (CRC press, 2015).
14. Rytov, S. Acoustical properties of a thinly laminated medium. *Sov. Phys. Acoust* **2,** 68–80 (1956).

15. Bannov, N., Aristov, V., Mitin, V. & Stroscio, M. A. Electron relaxation times due

to the deformation-potential interaction of electrons with confined acoustic phonons in a free-standing quantum well. *Phys. Rev. B* **51,** 9930 (1995).

16. Bannov, N. A., Vasko, F. T. & Mitin, V. V. Terahertz absorption by electrons and confined acoustic phonons in free-standing quantum wells. *Superlattices Microstruct.* **18,** 269 (1995).

17. Nishiguchi, N., Ando, Y. & Wybourne, M. N. Acoustic phonon modes of rectangular quantum wires. *J. Phys. Condens. Matter* **9,** 5751 (1997).

18. Balandin, A. & Wang, K. L. Significant decrease of the lattice thermal conductivity due to phonon confinement in a free-standing semiconductor quantum well. *Phys. Rev. B* **58,** 1544 (1998).

19. Lazarenkova, O. L. & Balandin, A. A. Electron and phonon energy spectra in a three-dimensional regimented quantum dot superlattice. *Phys. Rev. B* **66,** 245319 (2002).

20. Colvard, C. *et al.* Folded acoustic and quantized optic phonons in (GaAl) As superlattices. *Phys. Rev. B* **31,** 2080 (1985).

21. Chen, G. *Nanoscale energy transport and conversion: a parallel treatment of electrons, molecules, phonons, and photons*. (Oxford University Press, 2005).

22. Cahill, D. G. *et al.* Nanoscale thermal transport. II. 2003--2012. *Appl. Phys. Rev.* **1,** 11305 (2014).

23. Fonoberov, V. A. & Balandin, A. A. Giant enhancement of the carrier mobility in silicon nanowires with diamond coating. *Nano Lett.* **6,** 2442–2446 (2006).

24. Minnich, A. J. *et al.* Thermal conductivity spectroscopy technique to measure phonon mean free paths. *Phys. Rev. Lett.* **107,** 95901 (2011).

25. Yang, F. & Dames, C. Mean free path spectra as a tool to understand thermal conductivity in bulk and nanostructures. *Phys. Rev. B* **87,** 35437 (2013).

26. Regner, K. T. *et al.* Broadband phonon mean free path contributions to thermal conductivity measured using frequency domain thermoreflectance. *Nat. Commun.* **4,** 1640 (2013).

27. Zou, J. & Balandin, A. Phonon heat conduction in a semiconductor nanowire. *J. Appl. Phys.* **89,** 2932–2938 (2001).

28. Khitun, A., Balandin, A., Wang, K. L. & Chen, G. Enhancement of the

thermoelectric figure of merit of Si_{1-x} Ge_x quantum wires due to spatial confinement of acoustic phonons. *Phys. E Low-dimensional Syst. Nanostructures* **8,** 13–18 (2000).

29. Li, D. *et al.* Thermal conductivity of individual silicon nanowires. *Appl. Phys. Lett.* **83,** 2934–2936 (2003).

30. Wingert, M. C. *et al.* Thermal conductivity of Ge and Ge-Si core-shell nanowires in the phonon confinement regime. *Nano Lett.* **11,** 5507–5513 (2011).

31. Johnson, W. L. *et al.* Vibrational modes of GaN nanowires in the gigahertz range. *Nanotechnology* **23,** 495709 (2012).

32. Torres, C. M. *et al.* Observations of confined acoustic phonons in silicon membranes. *Phys. status solidi* **1,** 2609–2612 (2004).

33. Cuffe, J. *et al.* Phonons in Slow Motion: Dispersion Relations in Ultrathin Si Membranes. *Nano Lett.* **12,** 3569–3573 (2012).

34. Kakko, J.-P. P. *et al.* Fabrication of Dual-Type Nanowire Arrays on a Single Substrate. *Nano Lett.* **15,** 1679–1683 (2015).

35. Sandercock, J. R. Trends in brillouin scattering: Studies of opaque materials, supported films, and central modes. *Light Scatt. Solids III* **51,** 173–206 (1982).

36. Mutti, P. *et al.* in *Advances in Acoustic Microscopy* (ed. Briggs, A.) **1,** 249–300 (Springer US, 1995).

37. Casari, C. S. *et al.* Brillouin light scattering investigation of cluster-assembled carbon films: acoustic phonon propagation and elastic properties. *Diam. Relat. Mater.* **12,** 856–860 (2003).

38. Demokritov, S. O., Hillebrands, B. & Slavin, A. N. Brillouin light scattering studies of confined spin waves: linear and nonlinear confinement. *Phys. Rep.* **348,** 441–489 (2001).

39. Kuanr, B. K. *et al.* Spin-wave modes and line broadening in strongly coupled epitaxial Fe/Al/Fe and Fe/Si/Fe trilayers observed by Brillouin light scattering. *J. Appl. Phys.* **93,** 3427–3434 (2003).

40. Koski, K. J. & Yarger, J. L. Brillouin imaging. *Appl. Phys. Lett.* **87,** 61903 (2005).

41. Sato, A. *et al.* Anisotropic propagation and confinement of high frequency phonons in nanocomposites. *J. Chem. Phys.* **130,** 111102 (2009).

42. Graczykowski, B. *et al.* Hypersonic phonon propagation in one-dimensional surface phononic crystal. *Appl. Phys. Lett.* **104,** 1–5 (2014).

43. Sato, A. *et al.* Cavity-type hypersonic phononic crystals. *New J. Phys.* **14,** 113032 (2012).

44. Parsons, L. C. & Andrews, G. T. Off-axis phonon and photon propagation in porous silicon superlattices studied by Brillouin spectroscopy and optical reflectance. *J. Appl. Phys.* **116,** 33510 (2014).

45. Olsson, K. S. *et al.* Temperature dependence of Brillouin light scattering spectra of acoustic phonons in silicon. *Appl. Phys. Lett.* **106,** 51906 (2015).

46. Shin, H. *et al.* Tailorable stimulated Brillouin scattering in nanoscale silicon waveguides. *Nat. Commun.* **4,** (2013).

47. Blakemore, J. S. Semiconducting and other major properties of gallium arsenide. *J. Appl. Phys.* **53,** R123–R181 (1982).

48. Jogai, B. Three-dimensional strain field calculations in multiple InN/AlN wurtzite quantum dots. *J. Appl. Phys.* **90,** (2001).

49. Schulz, S., Caro, M. A., O'Reilly, E. P. & Marquardt, O. Symmetry-adapted calculations of strain and polarization fields in (111)-oriented zinc-blende quantum dots. *Phys. Rev. B* **84,** 125312 (2011).

50. Loudon, R. Theory of surface-ripple Brillouin scattering by solids. *Phys. Rev. Lett.* **40,** 581–583 (1978).

51. Sandercock, J. R. Brillouin-Scattering Measurements on Silicon and Germanium. *Phys. Rev. Lett.* **28,** 237–240 (1972).

52. Pokatilov, E. P., Nika, D. L., Askerov, A. S. & Balandin, A. A. Size-quantized oscillations of the electron mobility limited by the optical and confined acoustic phonons in the nanoscale heterostructures. *J. Appl. Phys.* **102,** 54304 (2007).

53. Nika, D. L., Cocemasov, A. I., Crismari, D. V & Balandin, A. A. Thermal conductivity inhibition in phonon engineered core-shell cross-section modulated Si/Ge nanowires. *Appl. Phys. Lett.* **102,** 213109 (2013).

54. Zen, N., Puurtinen, T. A., Isotalo, T. J., Chaudhuri, S. & Maasilta, I. J. Engineering thermal conductance using a two-dimensional phononic crystal. *Nat. Commun.* **5,** (2014).

55. Klemens, P. G. Theory of lattice thermal conductivity: Role of low-frequency phonons. *Int. J. Thermophys.* **2,** 55–62 (1981).

56. Wang, Z. & Mingo, N. Diameter dependence of SiGe nanowire thermal conductivity. *Appl. Phys. Lett.* **97,** 101903 (2010).

Chapter 5

Summary

The phonon states in crystal lattices can undergo changes induced by external boundaries. Modification of the acoustic phonon spectrum in structures with periodically modulated elastic constant or mass density – referred to as phononic crystals – has been proven experimentally and utilized in practical applications. However, ability of modifying the acoustic phonon spectrum in individual nanostructures via spatial confinement needs to be proven experimentally. Tuning the acoustic phonons in nanostructures via induced spatial boundary condition would bring tremendous benefits for controlling phonon-electron interaction and thermal conduction at the nanoscale. Recent technological developments suggest that tuning the phonon energy dispersion may become as important for the next generation of nanoelectronic circuits as engineering of the electron dispersion. Acoustic phonons carry heat in semiconductors. Improving phonon transport in nanometer scale devices is crucial for their reliability. Phonons set performance limits for alternative technologies under development, from superconducting electronics to spintronics and quantum computing.

Establishing the existence of confined phonon subbands in free-standing nanostructures, and determining the length scale, *D*, at which they reveal themselves are important tasks. In this dissertation, we reported measurements of the acoustic phonon spectrum of NWs and nanoporous membranes to conclusively prove the existence of the confined phonon polarization branches in individual nanostructures. More importantly, we

have also discovered that the phonon confinement effects become pronounced at a substantially larger length scale than previously believed (e.g. one order of magnitude larger than grey MFP in GaAs NWs). The obtained results can lead to more efficient nanoscale control of acoustic phonons, with benefits for various practical applications.